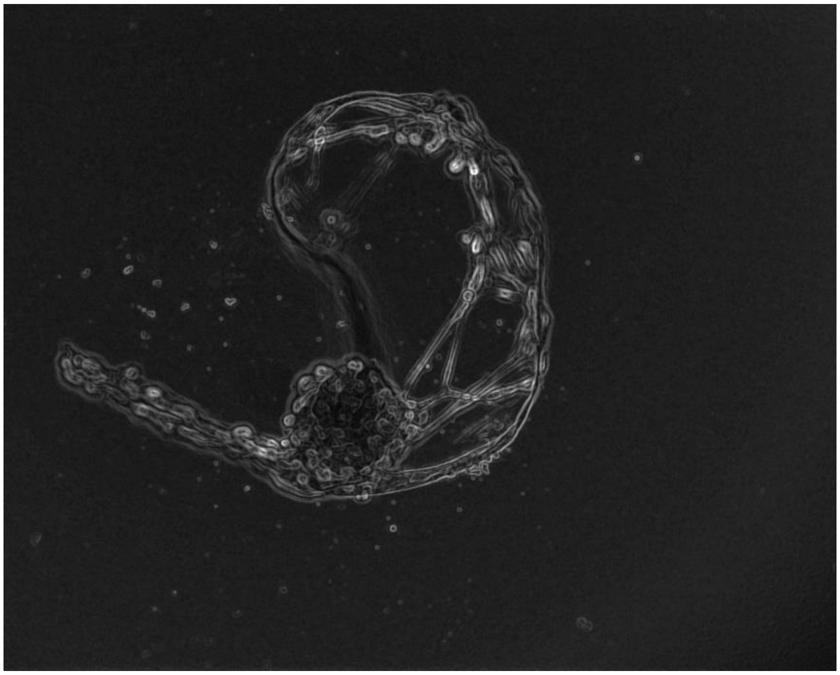

IMAGE GUIDED BRAIN CANCER MODELING

The Role of Promyelocytic Leukemia Protein in Glioblastoma Physiology

M.Sc. THESIS

MARIA TAMPAKAKI

“Brain and Mind Graduate Programme”

University of Crete, School of Medicine

Heraklion, 2019

EVALUATION COMMITTEE

EVANGELOS SAKKALIS, PRINCIPAL INVESTIGATOR	**SUPERVISOR**
KYRIAKI SIDIROPOULOU, ASSISTANT PROFESSOR	**EVALUATOR**
THOMAS MARIS, ASSOCIATE PROFESSOR	**EVALUATOR**

CONTENTS

ABSTRACT

Glioblastoma is the most malignant brain cancer among adults, according to the World Health Organization (WHO). It is characterized by excessive proliferation and infiltration, along with extensive inter- and intra-tumoral heterogeneity. Current standard therapy includes maximal safe surgical resection, followed by concurrent radiation and/or Glioblastoma adjuvant chemotherapy. However, in spite of intensive treatment, patients have a poor prognosis, due to the high recurrence potential of Glioblastoma. Identifying Glioblastoma biomarkers could help diagnose the disease earlier, characterize specific features regarding the tumor physiology and aggressiveness and even help in building new therapeutic strategies.

There is recent evidence suggesting, high expression of the Promyelocytic Leukemia Protein (PML), a tumor suppressor and cell regulator, in primary Glioblastoma samples. PML is expressed in all tissues and implicated in various ways to cancer biology. In brain, PML participates in the physiological migration of the neural progenitor cells, which have been also hypothesized to serve as the cell of origin of Glioblastoma. Recent studies in PML knocked-down mice indicate a common PML-mediated migratory pathway in both adult neurogenesis and Glioblastoma invasion within the central nervous system.

In this work, the invasive capacity of the well-described T98G and U87MG Glioblastoma cell lines is being explored. The role of PML in Glioblastoma pathophysiology, regarding the cell growth and invasive properties of the tumor, is investigated under PML overexpression in the U87MG cells. A combined *in vitro-in silico* approach is presented by using three dimensional biological models and translating biological observations in order to initialize, parametrize and validate a discrete mathematical model. The PML-mediated effects are estimated and visualized using conventional optical, along with light sheet fluorescence and confocal microscopy and the Glioblastoma tumor evolution is simulated *in silico*, in order to differentiate the observed biological phenomena.

Our overall findings indicate that PML overexpression suppresses cell proliferation, while it induces the invasive capacity of the U87MG Glioblastoma cells, by regulating distinct cellular mechanisms. Elucidating further the role of PML in Glioblastoma physiology could set PML as a potential biomarker of the tumor physiology and as a therapeutic target aiming at eliminating multiple sub-clones depending on their proliferative and/or invasive phenotype within the heterogeneous Glioblastoma tumor mass.

ΠΕΡΙΛΗΨΗ

Το Γλοιοβλάστωμα είναι καρκίνος του εγκεφάλου και σύμφωνα με τον Παγκόσμιο Οργανισμό Υγείας θεωρείται ο πιο δυσμενής και κακοήθης καρκίνος του εγκεφάλου για τον άνθρωπο. Όπως κάθε καρκίνος χαρακτηρίζεται από ακατάσχετο πολλαπλασιασμό και διήθηση καθώς και από πολύ υψηλή ετερογένεια. Η θεραπεία που ακολουθείται μέχρι στιγμής για την αντιμετώπιση του όγκου είναι η ασφαλέστερη δυνατή ολική αφαίρεση του καρκινικού ιστού, η οποία στη συνέχεια ακολουθείται από χημειοθεραπεία. Ωστόσο, το προσδόκιμο όριο των ασθενών με Γλοιβλάστωμα παραμένει πολύ χαμηλο, καθώς υπάρχει υψηλή πιθανότητα υποτροπής. Η ταυτοποίηση βιο-δεικτών για το Γλοιβλάστωμα θα μπορούσε δυνητικά να συμβάλει στην καλύτερη και έγκαιρη διάγνωση της νόσου, καθώς και στον προσδιορισμό συγκεκριμένων χαρακτηριστικών της φύσης του όγκου κάθε ασθενούς.

Πρόσφατες μελέτες αναδεικνύουν υψηλή έκφραση της πρωτεΐνης της Προμυελοκυταρικής Λευχαιμίας (ΠΜΛ) σε υψηλό ποσοστό πρωτογενών δειγμάτων ασθενών με Γλοιβλάστωμα. Η ΠΜΛ είναι μια ογκοκατασταλτική πρωτεΐνη, η οποία έχει φυσιολογικό ρόλο κυτταρικού ρυθμιστή. Εκφράζεται σε όλους τους ιστούς του οργανισμού και έχει συσχετιστεί με διάφορους τύπους καρκίνου. Στον εγκέφαλο, η ΠΜΛ συμμετέχει στη φυσιολογική μετανάστευση των νευροβλαστών κατά τη νευρογένεση, από τον κροταφικό στον οσφρητικό λοβό, όπου και διαφοροποιούνται. Σύμφωνα με θεωρίες που περιγράφουν την ανάπτυξη του Γλοιβλαστώματος, θεωρείται ότι οι νευροβλάστες ανήκουν σε μια ομάδα κυττάρων, τα οποία δυνητικά μπορούν να συντελέσουν ως τα αρχικά κύτταρα από τα οποία προκύπτει η νόσος. Πρόσφατες έρευνες σε γονιδιακά ανασυνδυασμένα ποντίκια στα οποία αποσιωπείται η έκφραση της ΠΜΛ, προτείνουν ότι η φυσιολογική κυτταρική μετανάστευση κατά την νευρογένεση και η διήθηση των κυττάρων στο Γλοιοβλάστωμα ενδέχεται να ελέγχονται από ένα κοινό κυτταρικό μονοπάτι το οποίο ελέγχεται από την ΠΜΛ.

Σε αυτήν την εργασία, μελετάται η διηθητική ικανότητα των T98G και των U87MG Γλοιοβλαστωματικών κυτταροσειρών. Στη συνέχεια εξερευνάται ρόλος της πρωτεΐνης ΠΜΛ στην παθοφυσιολογία του Γλοιοβλαστώματος όσον αφορά την ανάπτυξη και τη διήθηση του όγκου όταν αυτή υπερεκφράζεται. Στην παρούσα δουλειά ακολουθείται μια *in vitro-in silico* προσέγγιση, στην οποία χρησιμοποιήθηκαν τρισδιάστατα βιολογικά μοντέλα και μετάφραση των φαινομένων, με σκοπό την αρχικοποίηση, παραμετροποίηση και επικυρωποίηση ενός προβλεπτικού μαθηματικού μοντέλου για τον καρκίνο. Τα βιολογικά φαινόμενα μελετήθηκαν με τεχνικές συμβατικής, καθώς και συνεστιακής φθορίζουσας μικροσκοπίας και μικροσκοπίας λεπτής δέσμης φύλλου φωτός. Στη συνέχεια, η ανάπτυξη του όγκου προσομοιώθηκε

υπολογιστικά με σκοπό την διακριτοποίηση και απομόνωση των φαινομένων που παρατηρήθηκαν.

Τα ευρήματα αυτής της δουλειάς υποδεικνύουν ότι η ΠΜΛ αναστέλλει την ανάπτυξη των καρκινικών κυττάρων Γλοιοβλαστώματος και ενισχύει την μεταναστευτική τους ιδιότητα μέσω διαφορετικών, διακριτών κυτταρικών μηχανισμών. Η περαιτέρω μελέτη του ρόλου της ΠΜΛ στη φυσιολογία του Γλοιοβλαστώματος θα μπορούσε να αναδείξει την πρωτεΐνη αυτή ως πιθανό βιο-δείκτη για τη διάγνωση και το χαρακτηρισμό του όγκου. Ακόμη, η ταυτοποίηση του ρόλου της ΠΜΛ στην εξέλιξη του Γλοιοβλαστώματος μπορεί να την καταστήσει στόχο της αντικαρκινικής θεραπείας, με σκοπό να εξαλείψει τους διηθητικούς φαινοτύπους του όγκου που συχνά συντελούν στην υποτροπή της νόσου.

1. INTRODUCTION

Glioblastoma (GB) is the most malignant and aggressive primary brain tumor, classified as grade IV according to the World Health Organization (WHO; Louis et al., 2016). It is associated with a median survival of 12-15 months (Hou et al., 2006) and it can appear without a previous tumor diagnosis (primary) or through progression from lower grade tumors (secondary) (Mullins et al., 2013). GB most frequently occurs in frontal, temporal (Larjavaara et al., 2007; Zada et al., 2012) and cerebellar (Zada et al., 2012) regions, accounting for more than 60% of the adult brain tumors (Hanif et al., 2017).

GBs usually occur *de novo* (primary glioblastomas) in elderly patients, without exhibiting any signs of a previous less malignant lesion (Ohgaki and Kleihues, 2013). Secondary GBs, on the other hand, develop from a lower grade glioma usually of astrocytic nature (diffuse or anaplastic astrocytoma) and evident typically in younger patients (Ohgaki and Kleihues, 2013).

1.1. GB HETEROGENEITY

GBs are characterized by extensive inter-patient heterogeneity, exhibiting molecular and cellular diverse phenotypic profiles among patients (Aum et al., 2015). Furthermore, molecular and genetic intra-tumor heterogeneity has also been observed in GBs (Bonavia et al., 2011), creating multiple cellularly distinct sub-populations that coexist within the same tumor (Aum et al., 2015; Sun and Yu, 2015; Oraiopoulou et al., 2018). The different tumor clones can cooperate to help each other survive or compete for nutrients, oxygen and space, resulting in evolutionary prevalence of the best adjustable clone (Bonavia et al., 2011). Even though the wide heterogeneity in GB includes important information regarding the tumor evolution (Sun and Yu, 2015), it limits substantially the development of effective treatment (Aum et al., 2015; Sun and Yu, 2015; Oraiopoulou et al., 2018) and increases the possibility of recurrence (Aum et al., 2015).

1.2. GB MIGRATION, INVASION, INFILTRATION

On the microscopic-cellular level, the GB migrating cells have the ability to move, usually with the formation of specific membrane protrusions called invadopodia (Mallawaaratchy et al., 2015), and detach from the original tumor core spreading into the neighboring healthy brain tissue (Oraiopoulou et al., 2018). They preferentially travel along distinct anatomical structures pre-existing in the brain parenchyma known as “Scherer’s secondary structures” (Holland, 2000; Claes et al., 2007) which include the blood vessels, the meninges and the ganglia nerve tracts (Holland, 2000; Claes et al., 2007). GB invasion can be observed on the mesoscopic level and involves the process of direct expansion of the tumor bulk and penetration of GB migrating cells into the surrounding tissue (Koh et al., 2018). GB extra-cranial metastasis is rare (Nørøxe et al., 2016); however, in contrast to other brain tumors, infiltration is considered a typical clinical evidence of GB diffusion (Claes et al., 2007; Montana, 2016). This macroscopic process describes to ability of GB migrating cells to invade individually or in small clusters and diffuse into the adjacent healthy brain parenchyma (Claes et al., 2007; Montana, 2016).

1.3. CELL LINES

In order to study the GB tumor pathophysiology and identify specific molecular and cellular mechanisms contributing to oncogenesis or tumor maintenance, a variety of biological models have been applied in GB research (Grotzer et al., 2016; Klinghammer et al., 2017; Oraiopoulou et al., 2017, 2018). However, the evolutionary process that tumors undergo during clonal selection can only be approached with biological models that maintain the intrinsic tumoral heterogeneity (Mullins et al., 2013; Klinghammer et al., 2017; Oraiopoulou et al., 2018). Therefore, the latest trends in GB research employ patient-derived, primary cell lines, that better resemble the heterogeneous nature and the complexity of the disease and they are closer to the original tumor (Mullins et al., 2013; Oraiopoulou et al., 2017).

Secondary cell lines, on the other hand, have been extensively used in GB research since they are well profiled, easily manipulated (Klinghammer et al., 2017) and suitable to study specific cellular mechanisms (Klinghammer et al., 2017; Oraiopoulou et al., 2017) or to be used as a control of the patient-derived cells (Oraiopoulou et al., 2017, 2018). U87MG (Aaberg-Jessen et al., 2011; Oraiopoulou et al., 2017) and T98G (Stein, 1979; Matsumura et al., 2000) are two well-known GB secondary cell lines, which are representative of most common GB proliferative and invasive phenotypes and therefore often used in GB experimental models. Especially the T98G cell line is highly representative of the GB invasive behavior in *in vitro*, *ex vivo* and *in vivo* studies, due to cell-to-cell/matrix adhesion, epithelial-to-mesenchymal transition (EMT) and metabolic and microenvironmental factors (Ramão et al., 2012; Adamski et al., 2017). All secondary lines tend to differ from the tumor of origin due to clonal selection, hence they are characterized by less phenotypic heterogeneity and higher level of differentiation than the primary cell lines (Allen et al., 2016). Nonetheless, both the U87MG and the T98G cell lines are well-characterized and widely accepted as valid GB experimental models (Allen et al., 2016; Kiseleva et al., 2018).

1.4. PROMYELOCYTIC LEUKEMIA PROTEIN (PML)

1.4.a. PML GENERAL Characteristics

The promyelocytic leukemia protein (PML) was originally identified in acute promyelocytic leukemia (APL), as a chromosomal translocation between the chromosomes 15 and 17 (Hsu and Kao, 2018). In APL, PML fuses with the retinoic acid receptor alpha (RARα) and the hybrid protein inhibits the differentiation of the hematopoietic progenitor cells (Imani-Saber and Ghafouri-Fard, 2014).

1.4.b. PML KNOWN ISOFORMS

The PML transcript is organized into 9 exons (Figure 1) (Jensen et al., 2001; Hsu and Kao, 2018; Previati et al., 2018). Alternative splicing of the transcript can produce 7 isoforms of the protein which all share the same N-terminal regions, while they vary in the C-terminal part (Jensen et al., 2001; Hsu and Kao, 2018; Previati et al., 2018). The N-terminus of each isoform contains the RBCC or **TRI**partite **MO**tif (TRIM) which is a domain of several structurally conserved sequences including a Really Interesting New Gene (**R**ING) finger, two cysteine/histidine-rich **B**-Boxes (B1 and B2) and an α-helical **C**oiled-**C**oil domain (Jensen et al., 2001; Guan and Kao, 2015). PML known isoforms are classified into 7 categories based on their length (Jensen et al., 2001). They vary from PML I which is the longest isoform, to PML VII which is the shortest (Jensen et al., 2001).

PML I – VI are mostly located in the nucleus, with the exception of PML I that contains a Nuclear Export Signal (NES) located in exon 9 and therefore can also be found in the cytoplasm (Lallemand-Breitenbach and De The, 2010; Hsu and Kao, 2018; Previati et al., 2018). PML VII (Lallemand-Breitenbach and De The, 2010; Hsu and Kao, 2018; Previati et al., 2018), on the contrary, lacks exon 6 which contains the Nuclear Localization Signal (NLS), hence it is exclusively cytoplasmic. Remarkably, nuclear and cytoplasmic PML can present adverse activity depending on the environmental stimuli being exposed (Hsu and Kao, 2018). Apart from the classic PML I-VII proteins, alternative splicing of the PML transcript can also produce variants of the original isoforms classified as sub-type A, B or C, as shown in Figure 1**.** The different C-termini parts among the PML isoforms may indicate isoform-specific actions (Nisole et al., 2013).

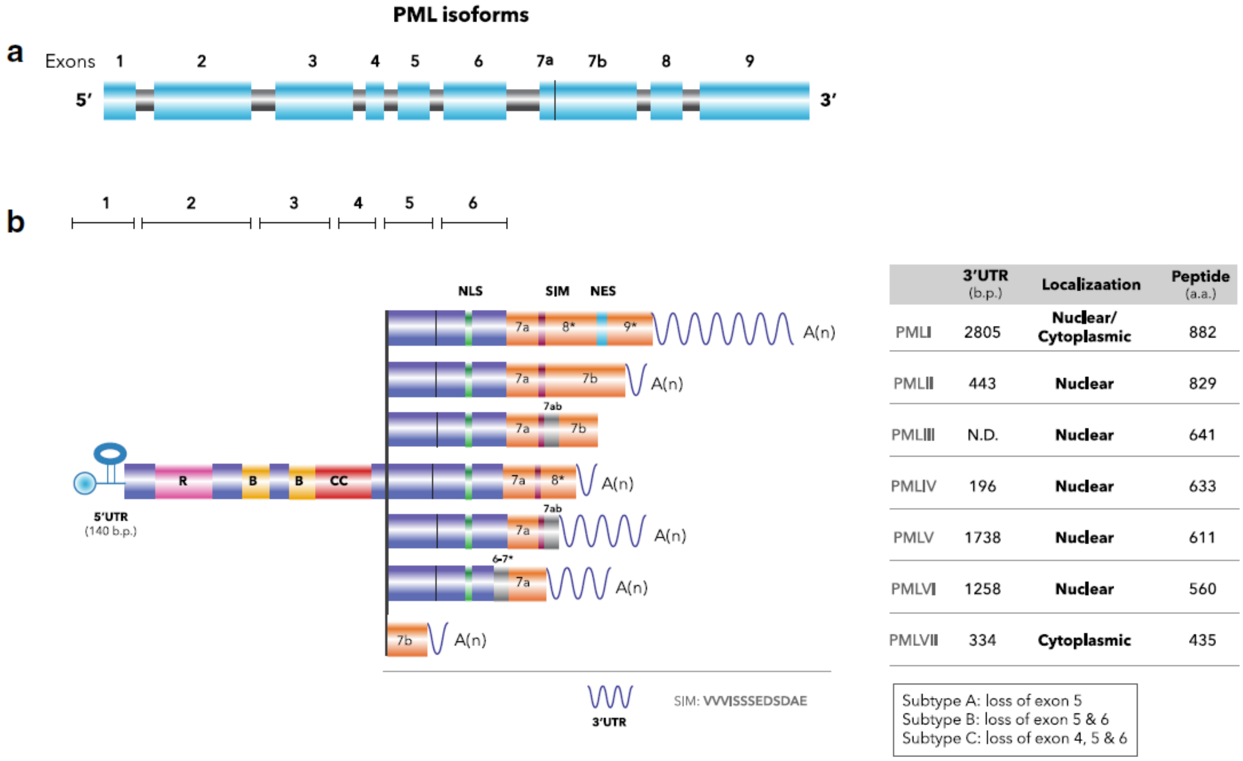

	3′UTR (b.p.)	Localizaation	Peptide (a.a.)
PMLI	2805	Nuclear/ Cytoplasmic	882
PMLII	443	Nuclear	829
PMLIII	N.D.	Nuclear	641
PMLIV	196	Nuclear	633
PMLV	1738	Nuclear	611
PMLVI	1258	Nuclear	560
PMLVII	334	Cytoplasmic	435

Subtype A: loss of exon 5
Subtype B: loss of exon 5 & 6
Subtype C: loss of exon 4, 5 & 6

Figure 1. Adopted by Hsu and Kao, 2018. Schematic representation of the PML gene organization, the alternative splicing of its isoforms and their localization.

1.4.c. PML NUCLEAR BODIES

STRUCTURE OF PML-NBS

PML is the essential organizer of the sub-nuclear structures called nuclear bodies (NBs) (Bernardi and Pandolfi, 2007; Lallemand-Breitenbach and De The, 2010; Guan and Kao, 2015). The NBs are protein structures interspersed in the interchromosomal space and anchored onto the nuclear matrix (Bernardi and Pandolfi, 2007; Lallemand-Breitenbach and De The, 2010). They are small nuclear foci with a diameter range from 0.1 to 1.0 um (Bernardi and Pandolfi, 2007; Lallemand-Breitenbach and De The, 2010; Guan and Kao, 2015). In most mammalian cells there are typically 5-30 present per nucleus depending on the cell type, phase of the cell cycle, differentiation stage (Bernardi and Pandolfi, 2007), stress and nutritional condition (Guan and Kao, 2015).

During NB-biogenesis, sumoylated PML molecules interact with each other through the SUMO-binding motif and recruit other proteins through sumoylation, protein-protein interactions or SUMO-binding domains (Bernardi and Pandolfi, 2007). PML forms the stable outer shell of the body and a number of mobile components including transcription and epigenetic factors, such as SP100 or DAXX, are usually located inside as shown in (Figure 2) (Bernardi and Pandolfi, 2007; Lallemand-Breitenbach and De The, 2010). PML-NBs are in general heterogeneous in terms of the PML isoforms they assemble; however there are indications underlying the existence of PML-NBs that also have isoform-specific composition (Bernardi and Pandolfi, 2007).

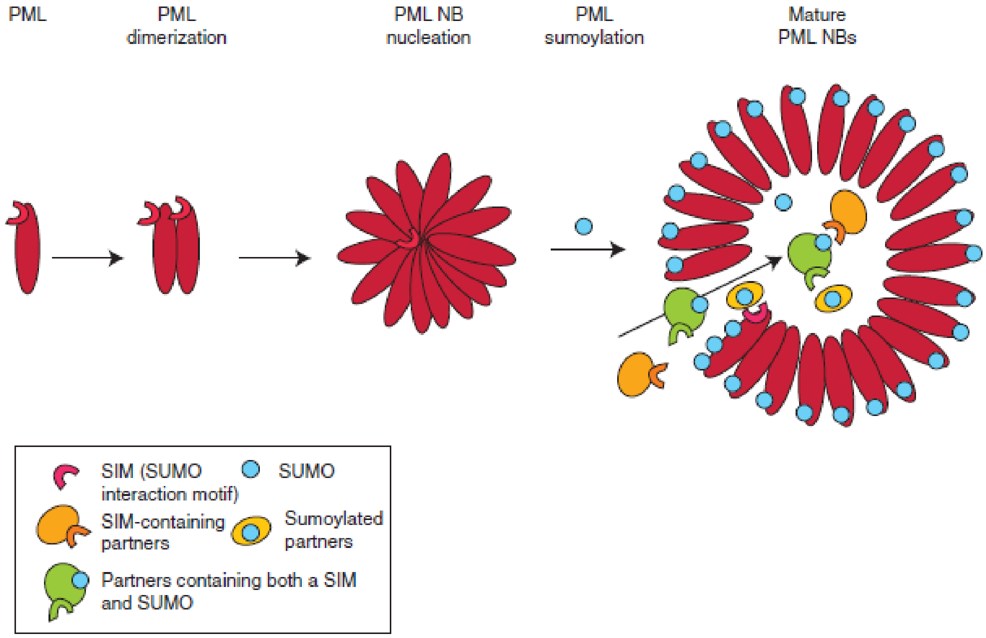

Figure 2. Adopted by *Lallemand-Breitenbach and De The, 2010*. Schematic representation of the PML-NBs nucleation. Sumoylatred PML proteins oligodimerize to form the shell of the PML-NB and attract other molecules inside the body via protein-protein or SUMO-binding interactions.

However, most of the PML protein molecules (over 90%) are freely diffused in the nucleus (Lallemand-Breitenbach and De The, 2010).

FUNCTIONS OF PML-NBS

PML and PML-NBs have been described as cell regulators with multiple roles in many physiological and pathophysiological conditions. They have been found to perform epigenetic modifications for the regulation of basic cellular functions such as transcription, apoptosis/senescence and DNA-damage repair, anti-viral protection, normal or cancerous stem cells fate (Lallemand-Breitenbach and De The, 2010; Mazza and Pelicci, 2013; Hsu and Kao, 2018; Previati et al., 2018), drug resistance (Hsu and Kao, 2018) and angiogenesis (Figure 3) (Mazza and Pelicci, 2013; Hsu and Kao, 2018). The models describing PML-NBs action mainly categorize their actions in three basic groups: identification and storage of proteins, post-translational modification of proteins and regulation of nuclear processes (Bernardi and Pandolfi, 2007).

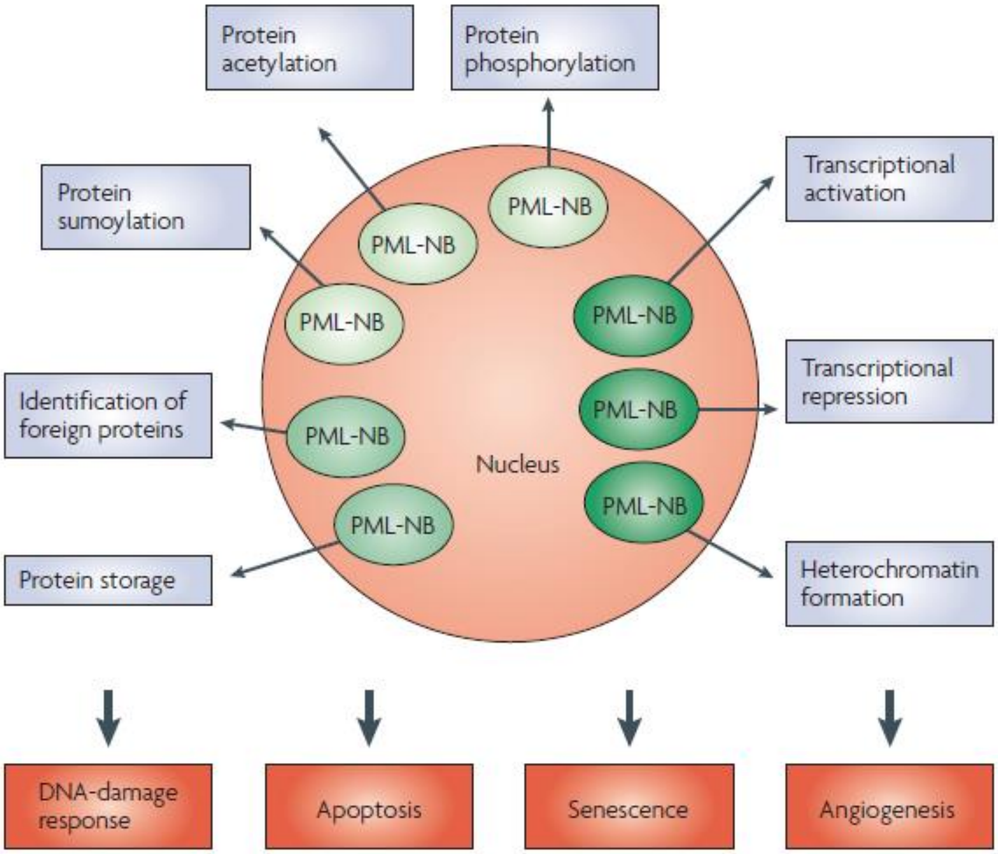

Figure 3. Taken by *Bernardi and Pandolfi, 2007*. The role of the PML-NBs and their many cellular functions.

1.4.d. PML IN BRAIN

Apart from APL, modifications in PML expression have been associated with various types of malignancies such as breast (Martín-Martín et al., 2016) and gastric (Lee et al., 2007) cancer. However, the specific role of PML in cancer remains yet to be unraveled, since PML can have both tumor-promoting or tumor-inhibiting effects regarding the type or the tissue origin of the tumor (Lee et al., 2007; Martín-Martín et al., 2016). PML expression is often decreased in human malignancies, which contributes to the progression of the tumor (Mazza and Pelicci, 2013). However, there are cases, where PML overexpression (OE) enhances the aggressiveness and metastatic features of the tumor resulting in poor prognosis for the patient (Martín-Martín et al., 2016).

More specifically, in the brain, PML has been shown to participate in the forebrain development (Regad et al., 2009; Kaneko et al., 2010). It has been found that PML expression is limited to the Neural Progenitor/Stem Cells (NPCs) in the developing mouse cortex (Regad et al., 2009) and it regulates the NPC physiological migration from the Sub-Ventricular Zone (SVZ) to the Olfactory Bulb (OB) through the Rostral Migratory Stream (RMS) (Figure 4) (Amodeo et al., 2017). This NPC-migration is achieved via a PML-mediated suppression of *Slits* (Amodeo et al., 2017) which are fundamental components in brain circuits development and axon guidance (Blockus and Chédotal, 2014) especially during SVZ neurogenesis (Kaneko et al., 2010). PML controls the PML/Slit axis via the Polycomb repressive complex 2 (PRC2) (Amodeo et al., 2017). The functional catalytic subunit of PRC2 is the Enhancer of zeste homolog 2 (EZH2) along with the two other proteins SUZ12 and EED and catalyzes the lysine H3K27 methylation resulting in heterochromatin regulation (Margueron and Reinberg, 2011).

Neurogenesis and GB expansion follow common migratory routes (Cuddapah et al., 2014; Faiz et al., 2015) and there is evidence that these two processes also share common cellular pathways such as the PML/Slit migratory axis (Amodeo et al., 2017). Interestingly, the migrating NPCs are also hypothesized to serve as the cell of origin for malignant gliomas in the adult mouse brain (Zong et al., 2015), indicating a potential role of PML in GB pathophysiology. In line with these observations, PML is often blocked in high grade (grade III or IV) tumors of the Central Nervous System (CNS), and this loss is usually connected with the tumor aggressive progression (Gurrieri et al., 2004; Mazza and Pelicci, 2013). However, there are studies indicating high PML expression in GB (grade IV) primary tumors (Gurrieri et al., 2004; Iwanami et al., 2013). In particular, in these cases PML has been shown to decelerate the cell cycle by extending the G1 phase (Iwanami et al., 2013), while it induces migration (Amodeo et al., 2017). More specifically, high levels of PML in primary GB cultures have been found to inhibit proliferation (Iwanami et al., 2013), whereas loss of PML in neural stem cells resulted in increased neurosphere diameter (Amodeo et al., 2017).

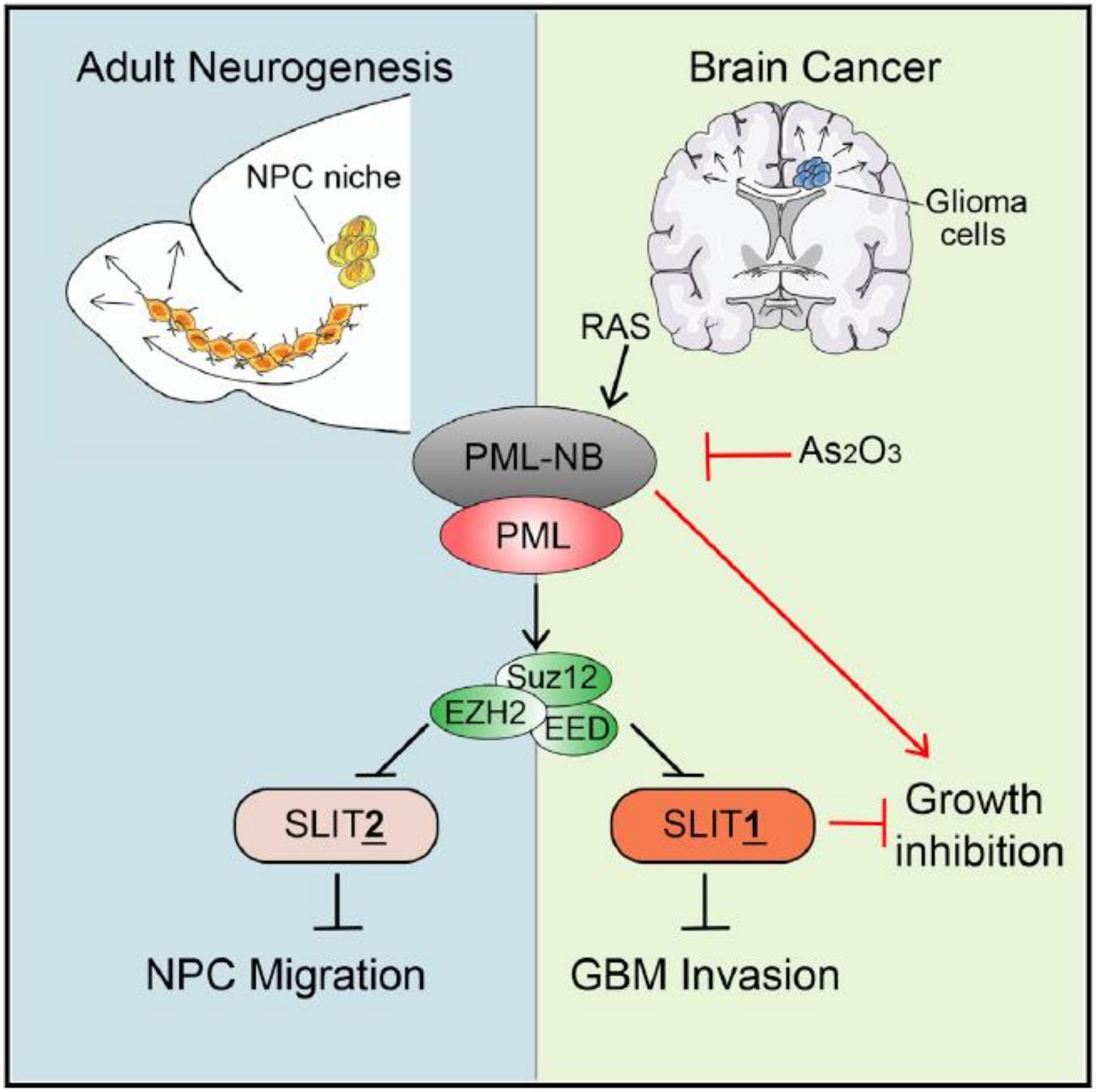

Figure 4. Taken by *Amodeo et al., 2017*. PML-mediated pathways in neuronal growth and migration.

1.5. IMAGING THE TUMOR PROPERTIES

In order to monitor a biological phenomenon, there is a critical need for advanced imaging techniques that allow the quantitative identification of translational biomarkers. There is a broad spectrum regarding the imaging biomarkers for many aspects of the tumor physiology and microenvironment, such as cell death and proliferation, cell motility and distribution, ECM components etc., which can provide information about the aggressiveness of the tumor or drug-treatment response (Kalinski, 2017). There are several approaches utilizing a variety of modalities for this purpose ranging from conventional and confocal microscopy to Light Sheet Fluorescent Microscopy (LSFM) or Single-Plane Illumination Microscopy (SPIM) and Optoacoustics microscopy that are able to capture the dynamic changes during the progression of the tumor overtime (Lorenzo et al., 2011; Mehrmohammadi et al., 2013; Taruttis et al., 2015; Psycharakis et al., 2018)

Conventional microscopy has been the basic imaging modality in biological research for decades. However, due to light scattering, the depth of the tissue visualization is limited and therefore requires very thin and small specimens (10-20um) or permanent fixation and tissue clearing of the sample for histological observation (Clendenon et al., 2011). Confocal or multiphoton microscopy, on the other hand, provide the capacity to non-invasively optically section a specimen and capture 2D images at different penetration depths that eventually enable the reconstruction of a 3D structure of an intact sample. This modality utilizes a spatial pinhole that rejects all the out-of-focus photons, in order to increase the optical resolution and contrast of a micrograph. The penetration depth achieved with confocal microscopy is close to 1mm with resolution under 1um being able to visualize processes at the subcellular level (Ntziachristos, 2010). However, the 2D raster scanning of the specimen with a single focused laser beam confines the borders of the field of view that can be imaged and often results in photobleaching and phototoxicity limiting the live cell imaging capacity of the technique (Dixit and Cyr, 2003; Bernas et al., 2004; Magidson and Khodjakov, 2013).

Compared to other fluorescent microscopy techniques, LSFM can image larger specimens and achieve deep tissue penetration depth, while still maintaining the high-resolution outcome (Santi, 2011). The biggest advantage of this technique is the potential of subcellular resolution imaging within a living sample with minimum photodamage (Lorenzo et al., 2011; Psycharakis et al., 2018). LSFM utilizes a thin plane of light (light sheet) that optically sections the specimen labeled with a fluorophore, at a plane perpendicular to the detection axis (Greger et al., 2007). It is a non-destructive modality since the sample is exposed to a very thin light sheet rather that a concentrated laser beam, providing excellent live sample imaging with resolution up to 10um (Verveer et al., 2007; Lorenzo et al., 2011).

Optoacoustic (or also known as photoacoustic; PA) microscopy is an emerging technology combining optical microscopy with ultrasound imaging (Ntziachristos, 2010; Mehrmohammadi et al., 2013). Its basic principle relies on reconstructing the source of an ultrasound wave, produced from the thermoelastic expansion of a contrast agent that absorbs energy from a laser-pulse propagating through the sample. An acoustic detector detects the ultrasound wave generated by the constant thermoelastic expansion and contraction of the light-pulse absorbing structures (Tserevelakis et al., 2016, 2017; Ovsepian et al., 2017). Since the sample is reconstructed based on the ultrasound detection, light scattering does not limit the depth of PA imaging which can reach from 0.5mm up to several cm of penetration with resolution up to 5um (Ntziachristos, 2010). PA, as LSFM, causes minimum photodamage, therefore allowing deep tissue penetration live sample imaging with potential clinical impact (Mehrmohammadi et al., 2013; Zou et al., 2017; Karlas et al., 2019).

1.6. MATHEMATICAL AND COMPUTATIONAL MODELING

Cancer progression is a multiscale complex process that differs among different cancer types and patients. In order to better understand the phenomenon, mathematical models have been developed that aim to describe the underlying mechanisms involved, based on biological experiments (Anderson et al., 2006; Alfonso et al., 2017). They are a useful tool that can provide information regarding the identification of specific relationships during cancer development and eventually help in predicting the behavior of the phenomenon and its response to drug treatment (Bogdańska et al., 2017; McKenna et al., 2017). Computational implementation of those models helps in integrating information from biological and clinical data and evaluate predictions that can be experimentally *in silico* tested (Oraiopoulou et al., 2017, 2018). Furthermore, they can be used in personalized medicine for the clarification of the precise effects of specific chemotherapeutic agents in line with each patient’s progress and guide finding the most beneficiary therapeutic strategy for each patient (Ballesta et al., 2014; Bogdańska et al., 2017).

The mathematical approaches used to model a specific biological phenomenon can be categorized into continuous or discrete models. Continuous mathematical models are often used to describe the average behavior of tumor cells at the tissue or whole-body level (Swanson et al., 2011). Discrete or hybrid-discrete (HDC) mathematical approaches are often used to develop individual-cell based models, which focus on the single cell interactions addressing each cell independently and bridging the gap from cells to tissues and organs (Anderson et al., 2007; Kam et al., 2012).

1.7. AIM OF STUDY

In this work, we study the invasive physiology of the U87MG and the T98G cell lines. Followingly, we present an *in vitro-in silico* approach in order to better understand GB physiology under PML presence in the U87MG cell line. To simulate better the primary GB tumors, we use a custom-made U87MG-PML cell line, which is genetically modified to overexpress the PML protein. We study the PML-mediated effects regarding the tumor growth and invasive properties using 2D and 3D biological models. Conventional optical along with confocal and light sheet fluorescence microscopy are employed in order to estimate and visualize the phenomena. The biological observations are further used to initialize, parametrize and validate a cancer predictive computational model in order to isolate distinct cellular functions and study their underlying mechanisms. Our findings are in line with the literature and indicate that PML OE inhibits growth, while it positively regulates migration in the U87MG GB cells and we use *in silico* modeling to further propose a mechanism potentially underlying the PML-mediated regulation of migration.

2. METHODS

A combined *in vitro-in silico* methodology is followingly step by step described. First, the techniques used for the biological models generation are presented. The conventional optical, along with light sheet fluorescence and confocal microscopy protocols used are also explained. In the last section, the translation of the biological observations is shown, in order to initialize, parametrize and validate the discrete mathematical model used in this study.

2.1. CELL LINES

The well-established human GB cell lines U87MG (ATCC® HTB-14™) and T98G (ATCC® CRL-1690TM, USA) were used in this work. The cells were cultured in Dulbecco's modified Eagle medium (DMEM; Gibco,UK) supplemented with Ham's Nutrient Mixture F12, cytokines (FGF-EGF, Peprotech, UK) and B27 (ThermoFisher Scientific, UK), 10% heat-inactivated fetal bovine serum (FBS) and 50ug/ml gentamycin (PANREAC Applichem, Germany; a.k.a. DMEM++) and incubated in standard lab conditions (37 °C, 5% CO_2).

Generation of the PML-expressing Cell Line. The cells were lentivirusly transfected with an rtTA expressing plasmid (pLenti CMV rtTA3 Blast (w756-1) was a generous gift from Eric Campeau (Addgene plasmid # 26429; http://n2t.net/addgene:26429; RRID: Addgene_26429)). After blasticidin selection, they were further lentivirusly transfected with a plasmid carrying the PML isoform IV, C-terminally fused to the DsRed monomer (Clontech, Mountain View, CA, USA) fluorescent protein (cloned between Xbal and BamHI in PMA2780 (pMA2780 was a gift from Mikhail Alexeyev (Addgene plasmid # 25438; http://n2t.net/addgene:25438; RRID: Addgene_25438) (Alexeyev et al., 2010)). PML expression was controlled by the TET operator and induced upon activation of rtTA by the antibiotic doxycycline (DOXY). In order to induce the PML expression, DOXY was present in the culture medium at final concentration 0.001ug/ml over time. The control cell line was the U87MG-PML transfected cells in absence of DOXY (non-induced) along with the wild type non-transfected U87MG (U87MG-wt) cell line. The presence of the PML protein is visualized by the DsRed fluorophore illumination and the signal is dotted due to the PML-NBs formation within the cell nucleus. In (Figure 5) the DsRed expression is used to detect PML distribution and confirm PML-NBs formation using an inverted wide-field fluorescence microscope (Leica, Germany) at 20x magnification.

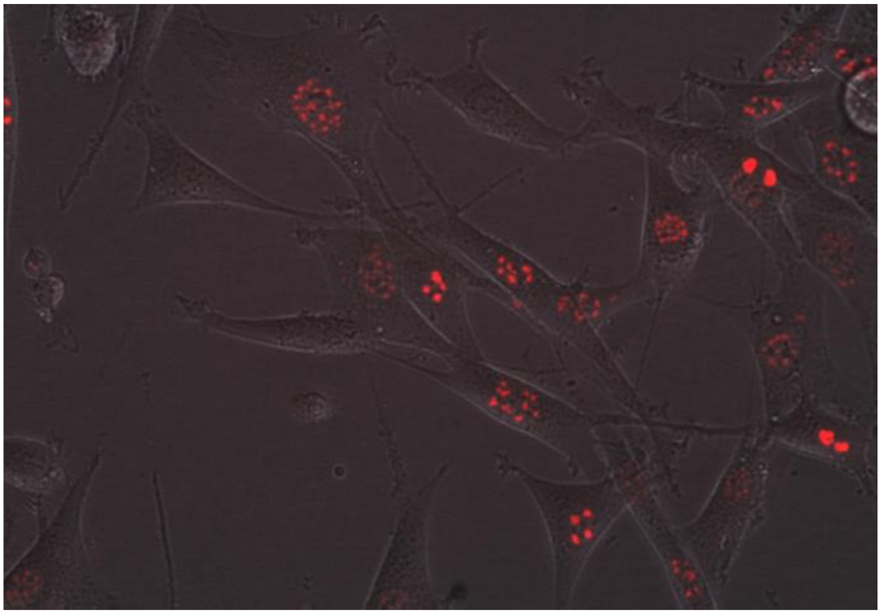

Figure 5. U87MG-PML OE cells in 2D culture at 10x magnification. The DsRed signal is dotted within the nucleus of the cell due to the PML-NBs formation. DsRed is shown in red.

2.2. 2D CELL CULTURES

2.2.a. CELL PROLIFERATION, CELL VIABILITY AND CYTOTOXICITY ASSAYS

Trypan Blue Exclusion. In order to determine the period of time required for the PML-expressing and the control cell lines to double in size and proliferate and their spontaneous cell death occurrence, a protocol adopted by Crowley et al., 2016 was performed. A single cell suspension of 1ml with cell density 20000 cells/ml of culture medium was seeded per well in a 24-well plate at day zero and the plate was incubated in standard lab conditions for 7 days. Every 24h after seeding, the culture medium of one well per cell type was removed and a single cell suspension was produced using trypsin-EDTA (Sigma-Aldrich, Germany) 1X solution. Followingly, the suspension of each cell type is added to 0.4% w/v trypan blue solution of equal volume. The basic principle of trypan blue staining relies on the fact that live cells have intact plasma membranes that can exclude various chemicals, including trypan blue. Dead or dying cells have ruptured plasma membranes, regardless of the mechanism of death, and therefore cannot exclude trypan blue and appear dark blue in brightfield (Srober, 2015). Thus, the cell concentration of each cell type was measured with a 24h interval using a hemocytometer and the spontaneous cell death percentage was estimated. The average growth rate and proliferation time of each cell line was estimated by applying an exponential linear regression model on the daily cell population data. The spontaneous cell death percentage was estimated as the average percentage of the dead cells compared to the whole cell population.

Fluorescence-Activated Cell Sorting (FACS). The cells were labeled with propidium iodide (PI) (PI-Sigma, Sigma-Aldrich, St. Louis, MO, USA), which binds to both DNA and RNA of late apoptotic or necrotic cells, while it is excluded from living cells (Rieger et al., 2011). Therefore, RNase is added before the PI to ensure that only DNA is stained. PI excitation was measured and analyzed using a BD flow cytometer (FACS, Becton Dickinson, USA). Cell-cycle estimations were also performed. The cells were fixed permanently using 70% ethanol and labeled using PI (Sigma-Aldrich, Germany). RNase is added before the PI to ensure that only DNA is stained. PI excitation is measured and analyzed using a FACS Calibur analyzer (BD Biosciences, San Jose, CA, USA), while the cell-cycle analysis is further performed using the ModFit LT software (Verity Software House, Topsham, ME, USA).

MTT Viability Assay. In order to assess the sensitivity to DZNeP (3-Deazaneplanocin A HCl) (Selleck Chemicals LLC (Houston, TX, USA)) of the PML-expressing and the non-expressing cell lines, the MTT viability assay was performed. For each cell type, a single cell suspension of approximate cell density 50000cells/ml of DMEM++ was seeded per well in a 24-well plate. The cells were treated with DZNeP (Selleck Chemicals LLC (Houston, TX, USA)) at a range of 0.05-40uM dissolved in DMSO (PanReac Applichem, ITW Reagents) and 1:1000 DMSO concentration was used as control. The plate was incubated in standard lab conditions until the control wells were approximately 90-100% confluent. Followingly, the culture medium was removed from all wells and replaced with 200ul MTT (Sigma M5655-1G, UK) working solution 1mg/ml final concentration dissolved in PBS 1X. The plate was incubated at 37^oC in darkness in CO_2 absence for ~3h. In principle, the yellow tetrazolium MTT (3-(4, 5-dimethylthiazolyl-2)-2, 5-diphenyltetrazolium bromide) is reduced by the mitochondrial dehydrogenases of the live cells to generate intracellular purple formazan crystals of NADH/NADPH insoluble in aqueous solutions (van Meerloo et al., 2011). Upon the formation of the crystals, they were solubilized in 300ul of acidified isopropanol and the optical absorbance of the solution was monitored at 595nm using a spectrophotometer. Repeated measurements at 660nm followed, for normalization over cell density. The dose-response curves were generated using the formula:

%growth inhibition= ((positive control-test value)*100)/positive control

The positive control corresponds to the viable cell population measurements of the untreated cells. The IC50 was defined as the drug concentration at which half of the cell population was inhibited.

2.3. 3D CELL CULTURES

2.3.a. GENERATION OF 3D MULTICELLULAR SPHEROIDS

3D multicellular spheroids were generated using the hanging-drop technique, as previously described in (Foty, 2011; Oraiopoulou et al., 2017). For each cell type, a single cell suspension of approximate cell density 625cells/50ul of DMEM++ was seeded per well in a 96-well hanging drop plate (3D Biomatrix, USA). Agarose solution 1% w/v was added in the reservoirs of the plate to prevent droplet evaporation. The growth pattern of the spheroids was monitored over time up to 21 days using a Leica DFC310 FX inverse wide-field optical microscope (Leica, Germany). The progress of all the invasive and the non-invasive spheroids was monitored over time using sequential brightfield images captured by optical microscopy. For all spheroids, the tumor core area was semi-automatically segmented from the image background in Matlab 6.1 (The MathWorks Inc., USA). Drug sensitivity was assessed in 3D spheroids by measuring the reduced areal expansion of the treated spheroids compared to the untreated control. The average growth curves were analyzed with Prism 5 software (GraphPad Software, Inc., USA) using regression analysis.

2.3.b. INVASION ASSAY

In order to study the invasive physiological characteristics of the different cell types, an invasion protocol previously described by Oraiopoulou et al., 2018 was performed. After Day 4 of the experimental procedure, the aggregation process was completed and the multicellular spheroids were transferred in a U-bottom plate within an ECM-like substrate. The invasion solution contained ice-cold BME Pathclear (Amsbio, Cultrex ®, UK) diluted in supplemented DMEM-F12 at final concentration 1:1. The U-bottom plate was centrifuged for 5min at 300rpm at 4°C, in order to place the spheroids at the center of each well, homogeneously distribute the invasive substrate and eliminate any bubbles within it. After 1h of incubation at 37°C for solidification of the invasive substrate, warm culture medium was added per well and replenished when needed. The expansion and the invasive morphology adopted by the spheroids was monitored over time using a Leica DFC310 FX inverse wide-field optical microscope (Leica, Germany). For the treated and non-treated invasive spheroids, the evolution of the overall invasive area was estimated by measuring the maximum radius that encloses all the invasive cells taken from the core center to the periphery as described in (Oraiopoulou et al., 2018) and shown in (Figure 6). To estimate the invasive rim, the radius of the core of the spheroid was subtracted from the radius of the whole invasive area. The cellular density of the invasive rim was semi-automatically estimated using the Ilastik software.

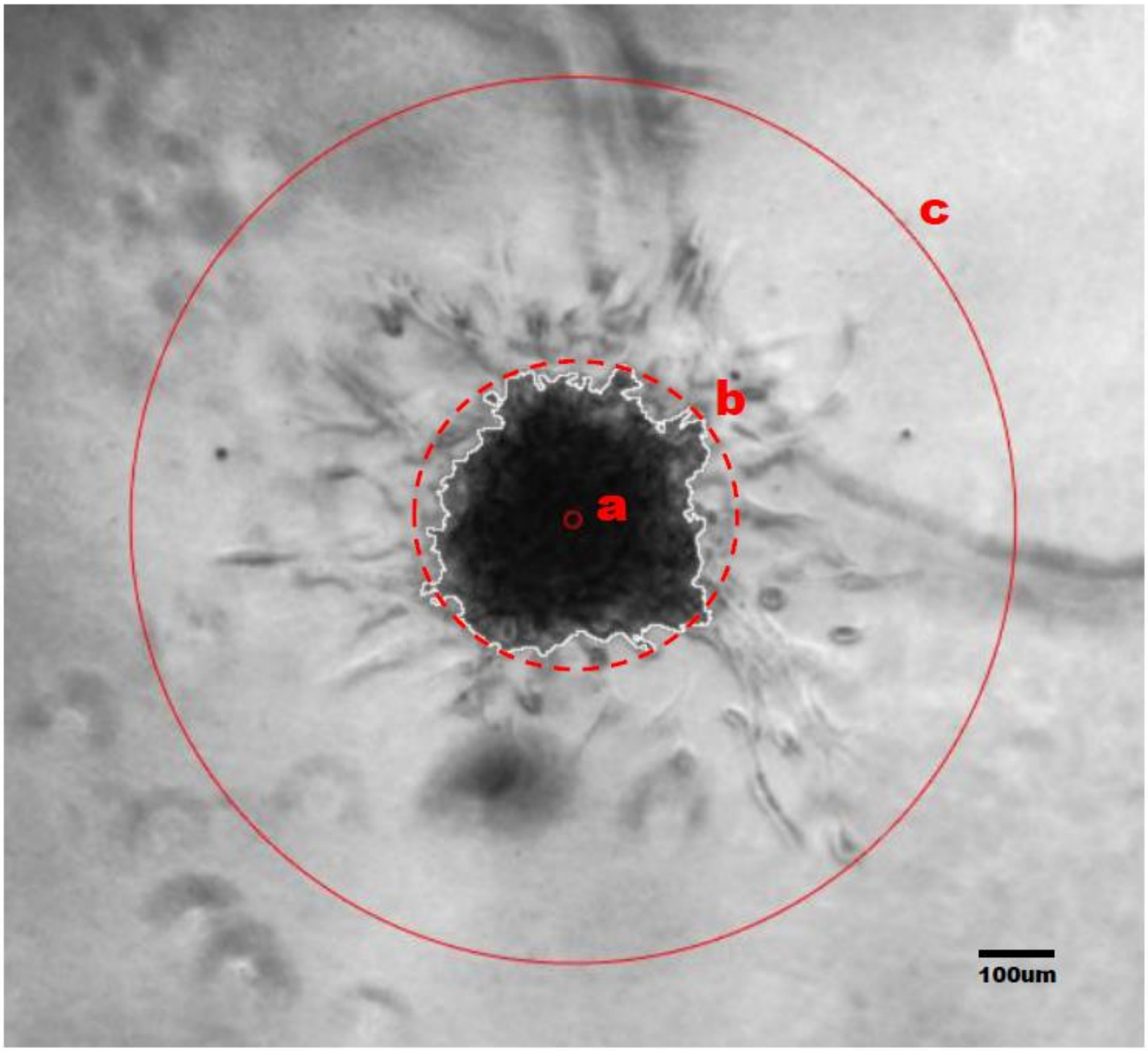

Figure 6. An illustration of the three procedural steps of the image analysis. By superimposing the segmented areas on a representative T98G invasive spheroid of Day 2, the core center (a) is semi-automatically depicted and the area of the core spheroid is shown as segmented on the Fiji software (b, white dotted). The radius of the core area is estimated (b, red), accordingly. Followingly, the maximum radius is fitted on the whole area (c). The invasive rim is measured accordingly by the subtraction of the core radius (b, red) from the whole invasive radius (c). Scale bar is set at 100μm.

2.4. LIGHT SHEET FLUORESCENCE AND CONFOCAL MICROSCOPY SCANNING

In order to better physiologically describe the growth and the invasive pattern of the cells under study, LSFM and confocal microscopy were employed using a custom built LSFM set-up and an LSM 710, AxioObserver (Carl Zeiss, Germany) confocal microscope at 10x magnification.

For the LSFM, a custom built set-up was used as shown in (Figure 7). The samples were transferred in Fluorinated Ethylene Propylene tubes (FEP-tubes; Bola, Germany), due to their refractive index which is similar to water. Each spheroid was imaged sequentially at 4 different projections (0o, 90o, 180o, and 270o) at two fluorescent channels. For confocal microscopy, μ-slide (ibidi, UK) plates were used. The spheroids were immobilized within the FEP-tubes or the μ-slide plates using CyGEL (Biostatus, UK) a thermoriversible gel that solidifies in warm environment and enables live imaging, introducing no noise during scanning. The invasive spheroids were cultured in BME diluted in supplemented DMEM-F12 as in (Oraiopoulou et al., 2018), which they were also allowed to invade over time. Culture medium was periodically added in the FEP-tube or the μ-slide plate whenever needed.

LSFM and confocal microscopy was used to monitor the death pattern of the spheroids using the DRAQ7 (Biostatus, UK) nuclear dye at 1:200 dilution. DRAQ7 is a far-red fluorescent nuclear probe that penetrates the membrane of necrotic or late apoptotic cells and binds to their nuclear DNA indicating cell death in non-fixed samples (Akagi et al., 2013). The spheroids were treated with DRAQ7 approximately 12-20h before the LSFM/confocal scan and excited at 635nm/643nm respectively. For the U87MG-PML OE cells, the PML expression was monitored using the DsRed monomer distribution. DsRed monomer was fused with the PML protein and therefore reported its presence and it was excited at 488nm/543nm for the LSFM and confocal scanning respectively. In addition, the cell-permeant 2', 7'-dichlorodihydrofluorescein diacetate (H_2DCFDA) (also known as dichlorofluores cin diacetate) was used as a counter stain, during confocal scans for the detection of the live cells. H_2DCFDA is a chemically reduced form of fluorescein often used as an indicator for reactive oxygen species (ROS) in cells (Wu and Yotnda, 2011). The spheroids were treated with H_2DCFDA approximately 10mins in the dark before confocal scanning and excited at 488nm.

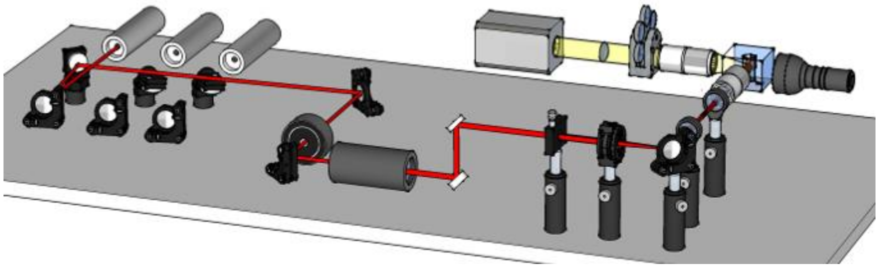

Figure 7. LSFM custom apparatus. The sample illumination is done perpendicularly to the direction of observation. The laser beam is introduced into the illumination path by using a set of flip mirrors. A cylindrical lens is used to form the laser beam in a plane of light and illuminate a thin region around the camera focal plane, as it is established orthogonally to the detection axis. Optical sectioning is performed as the sample is translated through the illuminated plane. In each measurement a stack of 50-80 optical sections is acquired. When different laser

sources are used (488nm and 635nm diode lasers), Multispectral imaging is achieved; different regions within an entire plane of the spheroid are selectively excited and their emission is separately acquired. For better illumination and deeper light penetration Multiview imaging is performed. The specimen is sequentially rotated to various angles compared to the initial position and thus more projections (views) are acquired (usually four orthogonal views).

Furthermore, for the proliferation detection in the T98G cells, the cells were treated using the PKH26 (Sigma-Aldrich, Germany) protocol by following the manufacturer's instructions, as well as transfected with green fluorescence protein (GFP) (Addgene, USA, a gift from Eric Campeau, (13)) or GFP linked to E-cadherin plasmids (Addgene, USA, a gift from Jennifer Stow, (14)). The cells were treated before plating with the lipophilic PKH26 red fluorescent (working solution of 4μl/ml buffer) which was used to monitor their proliferative history. Transfected cells were cytoplasmically expressing either GFP or GFP/E-cadherin. After the invasion assay, the spheroids were permanently fixed with 4% PFA and washed to remove the medium's phenol red. The T98G fixed spheroids were also treated with the nuclear dye Draq7 (Biostatus, UK) overnight at 1:200 dilution to label the nuclei. Followingly, T98G invasive spheroids were imaged using a LSM 710, AxioObserver (Carl Zeiss, Germany) confocal microscope in 10x and 40x magnification scanned at 543 nm (PKH26), 488 nm (GFP) and 640 nm (DRAQ7).

Confocal images were analyzed using Zeiss Zen lite blue edition software. For the LSFM images registration and fusion algorithms are applied to align and integrate the acquired projections into a final 3D image (Figure 8). The same procedure is repeated for both fluorescence channels, the resulting images are registered and combined to form the final volumetric multicolor isotropic image.

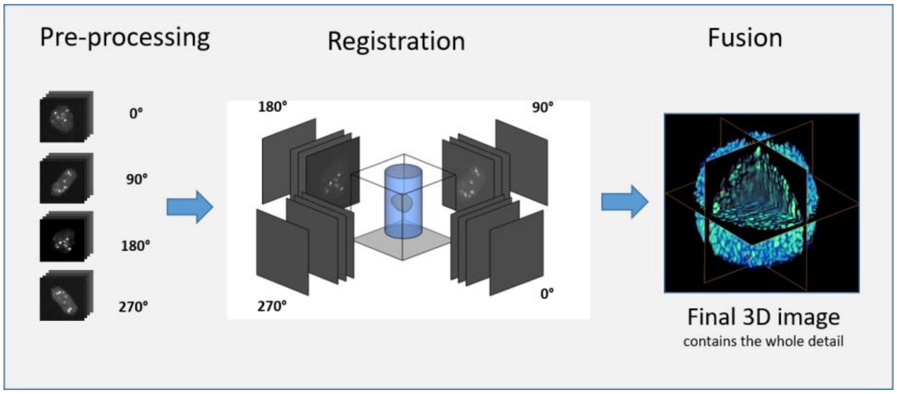

Figure 8. LSFM image analysis process.

2.5. MATHEMATICAL APPROACH AND COMPUTATIONAL DOMAIN

In order to describe the observed cell growth and invasion of the *in vitro* experiments, a simplistic discrete mathematical model was used to simulate the growth expansion of a planar slice through a 3D tumor spheroid. In the context of this model, each individual cell is described by a discrete cellular automaton (CA), which is capable of producing a variety of unexpected behaviors.

The mathematical approach in this work is based on the model originally proposed by Anderson, 2005. The model assumes discrete tumor cells which follow biologically driven rules and can locally interact with each other. Specifically, the tumor cells are allowed to grow and proliferate, as well as to move and migrate on a homogenous and constant scaffold. Following random selection, cells can either die or increase their age. Once proliferation age is reached, cells can divide or not divide (enter quiescence state) depending on whether there are empty adjacent sites. Heterogeneity of the tumor is considered only in terms of the cell population's adhesion properties, while all other properties are kept the same for all cells. The adhesive property of the cells is applied during cell movement and describes the cell's preference to bind with a variable number of other cells in its new position. It is assumed that cell properties are inheritable and intrinsic properties that are not regulated by the microenvironment.

2.5.a. PARAMETRIZATION OF THE MODEL

It is assumed that tumor cells lie within a Moore neighborhood on a regular 2D lattice that resembles a planar slice through the 3D multicellular spheroid. Lattice size L equals to 5mm and each *h* x *h* lattice site can accommodate only one cell which size h equals to 21.5um.

The **initial tumor size** is based on the initial spheroid size according to the *in vitro* estimations. The initial **cell density** resembles the compactness of the tumor at the first time point and estimates the cellularity of the initial tumor. The **proliferation time** of the cells is approximated by the relevant *in vitro* doubling time experiments. In order to proliferate, each cell must find an empty space for its daughter cell within the Moore neighborhood. If no vacancy is found in that area, the cell cannot divide (enters a quiescent state) and it keeps searching until an empty space is found and it immediately proliferates. **Proliferation handicap** corresponds to the number of empty sites +1 in its neighborhood that a cell requires in order to proliferate. Handicap number greater than zero, produces less dense tumors and allows cells to more easily become quiescent, thus reduces the growth expansion. Contact inhibition is simulated controlling the **proliferative depth** of the spheroid, which resembles the maximum distance (measured in cells) over which a cell is able to push other cells away in order to divide. To counter balance proliferation and death among different conditions, it is assumed that **random cell death** is a given percentage of the proliferation rate. **Drug mediated cell death** was examined as a function either dependent or not on proliferation rate both depended and independent phenomenon. Once a cell dies, the space empties immediately and new cells can take its place.

Cell movement is stochastic and can adopt different motility mechanisms triggered by different cell-to-cell adhesion forces. Cell motility was considered as a resultant of the cell's random **diffusive movement** capability, which was the same for the whole population, and its adhesive properties, which differed among phenotypes. Cells are allowed to move in empty neighboring locations in the Moore neighborhood according to the diffusion equation (1), adopted by Anderson, 2005, which is discretized to movement probabilities for each individual cell.

$$\frac{\partial c}{\partial t} = \overbrace{D_c \nabla^2 c}^{\text{diffusion}} \quad (1)$$

D_c and C denote the diffusion coefficient and the cancer cells concentration respectively. Their adhesive property will allow the cell to move, only if the population of the neighbors in the cells arriving location is equal to its preference. Cell movement according to the cell adhesion preference is illustrated in Figure 9.

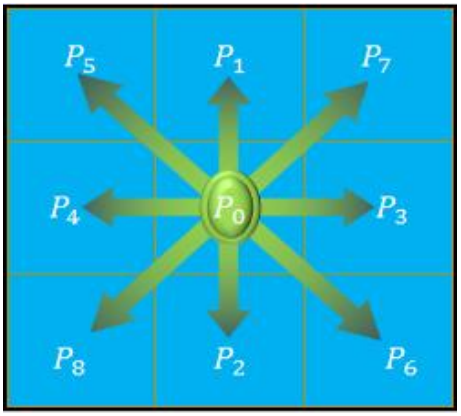

Figure 9. Stochastic cell movement illustration of the motile cell towards the arriving location.

An indicative brief description of the cell fate parallel processes of the developed model is depicted in Figure 10.

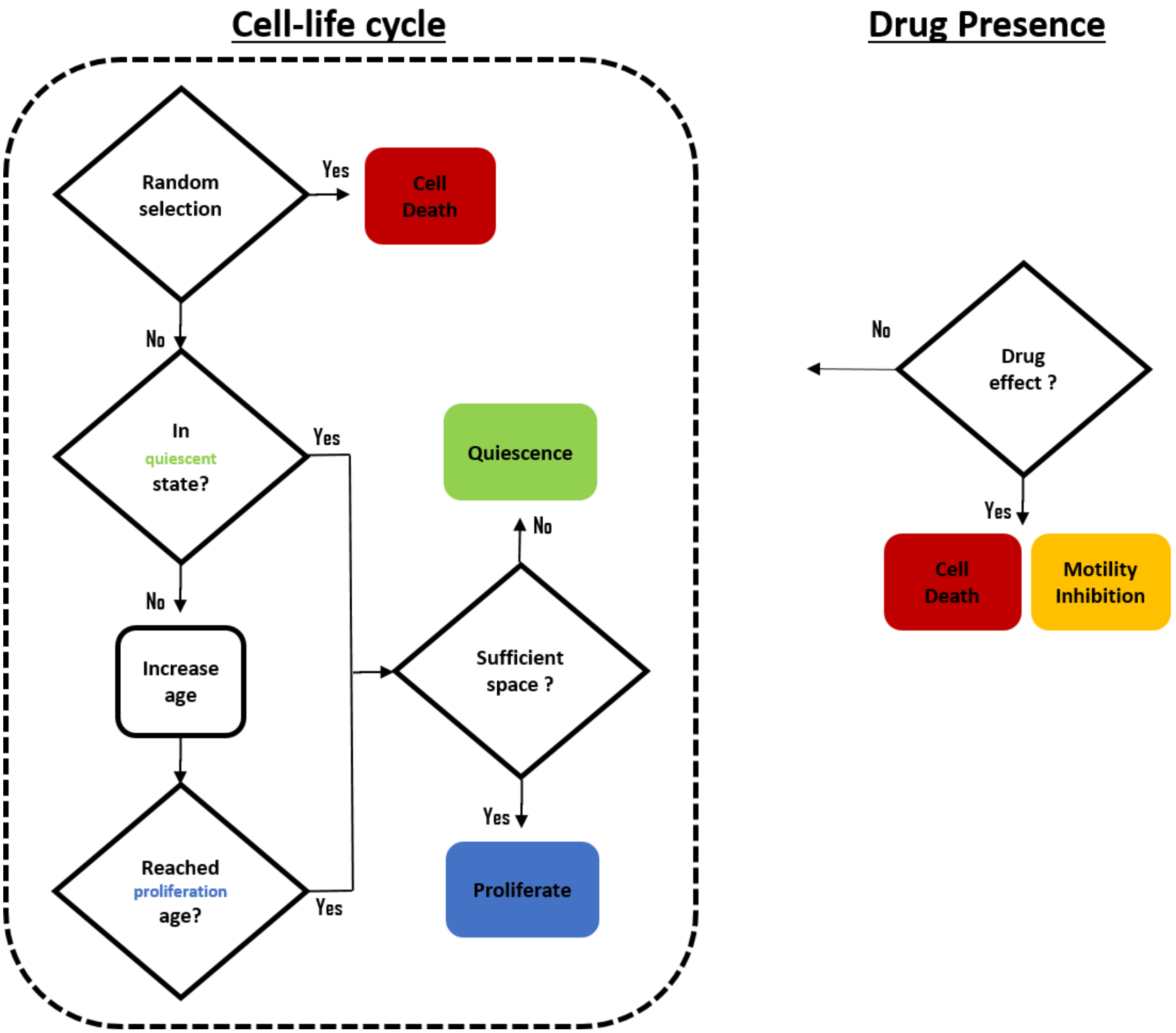

Figure 10. Flowchart of the two parallel cell fates in drug presence. In conditional absence of cell movement, only the cell life cycle processes (left) determine cell fate.

3. RESULTS

In this study the pathophysiology of an own-established U87MG-PML GB cell line was estimated regarding the growth and invasion tumor progress over time. The well-described U87MG-wt and T98G GB secondary cell lines were used as control. The growth properties were studied in both 2D and 3D conditions, while the invasive properties were studied exclusively in 3D, where cell migration was fully ECM-dependent. To further unravel the growth and invasive mechanisms upon PML OE, the sensitivity to DZNeP, an EZH2 histone methyltransferase inhibitor, was also estimated. A computational parameter study, along with a possible mechanistic explanation of the biological observations are given based on the computational simulations.

3.1 TUMOR GROWTH

3.1.a PROLIFERATION/DOUBLING TIME ESTIMATION

In principle, glioma cells double in size and proliferate, with a doubling time interval of 24-48h (Oraiopoulou et al., 2017). Specifically for the U87MG-wt cells, their population doubling time is estimated at ~30h as provider's recommendations ATCC® HTB-14™, USA and further reports (Oraiopoulou et al., 2017). Furthermore, the spontaneous cell death of the U87MG-wt has been reported at 6% (Hambsch et al., 2017). In this work the doubling time and cell viability of the own established U87MG-PML line was estimated in induced (U87MG-PML OE) and non-induced (U87MG-PML) condition.

The doubling time and cell viability of both cell lines was estimated in 2D cell cultures using the trypan blue exclusion viability assay. The measurements are represented in

Table 1 The average doubling time of the U87MG-wt and the T98G cell line was estimated at approximately 75h and 29.9h and the intrinsic cell death at 15% and 11.4% respectively. The proliferation time of the U87MG-PML cell line was estimated at approximately 90h and the intrinsic cell death at 10%. As expected, the U87MG-PML OE cells exhibited slower growth dynamics. Their doubling time was estimated approximately at 133h and their intrinsic cell death rate remained constant at 10%. The presence of the antibiotic did not significantly affect the growth pattern or the spontaneous cell death rate in either of the cell types.

FACS for cell-cycle analysis results were in line with trypan blue estimations and revealed a prolonged S-phase and reduced G2-phase in the U87MG-PML OE cells as it can be seen in Figure 11.

Cell Type	***Doubling Time (h)***	***Spontaneous Cell Death (%)***
U87MG-wt	75	15
T98G	29.9	11.4
U87MG-PML	90	20
U87MG-PML OE	133	20

Table 1. Doubling time and spontaneous cell death mean estimates for the GB studied cell lines

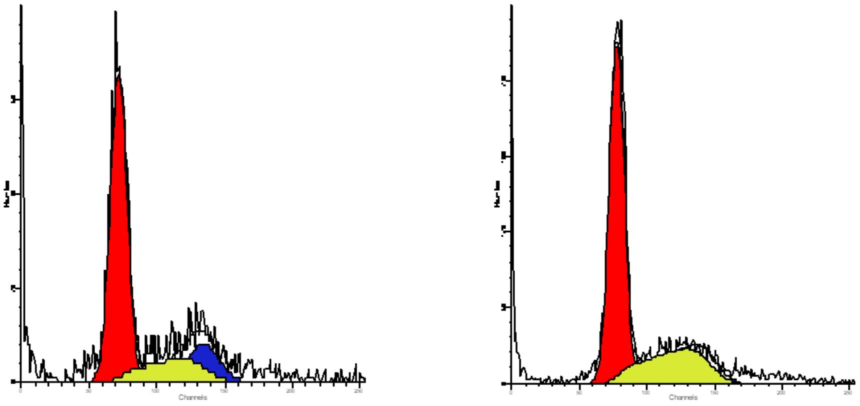

Figure 11. FACS for cell-cycle analysis for the U87MG-PML (left) and U87MG-PML OE (right) cell lines. With red, blue and green are represented the G1-phase, G2-phase and S-phase respectively.

3.1.b TUMOR GROWTH EXPANSION

In order to simulate the growth of an avascular GB tumor, 3D multicellular spheroids were generated using the hanging drop technique (Larson, 2015). Optical microscopy was used to monitor the growth of the spheroids over time. Bright field micrographs were captured in predefined time intervals, in order to estimate the area expansion of the tumor. This imaging approach, however, did not allow any quantitative measurements regarding the spheroidal cell density or the size, shape and polarity of the cells. In order to better assess the physiology of the growing 3D tumors, we used LSFM and confocal scans to visualize the cell death pattern and the PML distribution.

The U87MG-wt and the U87MG-PML /OE cells along with the T98G cells approximately needed 4 days from plating to spheroid formation (zero day). U87MG-PML OE cells exhibited slower aggregation capacity, with deformed tumor boundaries and less compactness as depicted in bright field images (Figure 12) and in confocal images (Figure 13). As it has been previously reported (Foty, 2011; Leung et al., 2015), the presence of an ECM-like substrate in low concentration within the growth environment of the spheroid enabled better cell adhesion and aggregation. Therefore, in order to facilitate the spheroid generation for comparison purposes among the cell types, we added 1% of BME Pathclear (Amsbio, Cultrex ®, UK) within the hanging drop, 2 days after seeding.

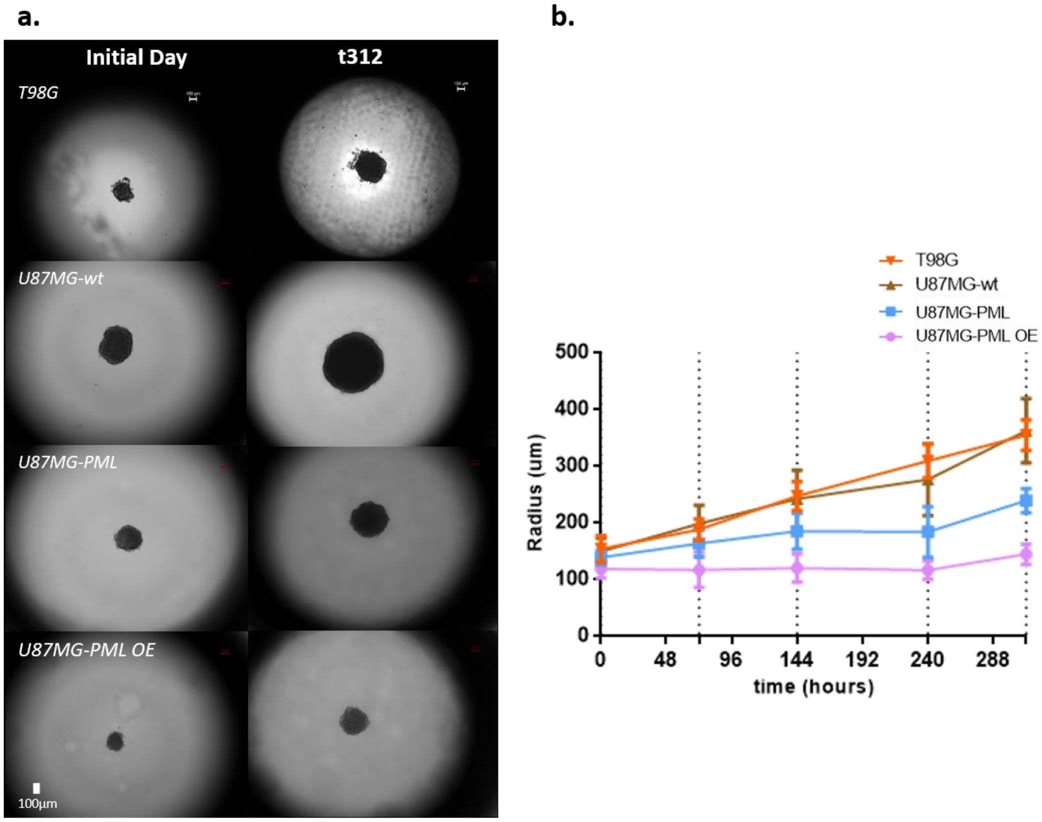

Figure 12. Growth expansion of the T98G, U87MG-wt, U87MG-PML and OE spheroids within the hanging-drop. (a) **Bright field images of the growth of the spheroids as in hanging-drops from the initial time point of spheroid formation and the final day of the experiment (initial day left column, final day right column). Scale bar is set at 100 microns.** (b) **Spatiotemporal evolution curves representing the radial expansion of the spheroids overtime.**

The bright field images depict the spheroids at the initial and the final time point in one plane of focus under the same acquisition parameters, while the growth curves represent the radial expansion over time, as estimated after the segmentation of the respective images. It can be observed that the U87MG-PML OE cells exhibited significantly slower growth dynamics, as also indicated in the 2D experiments.

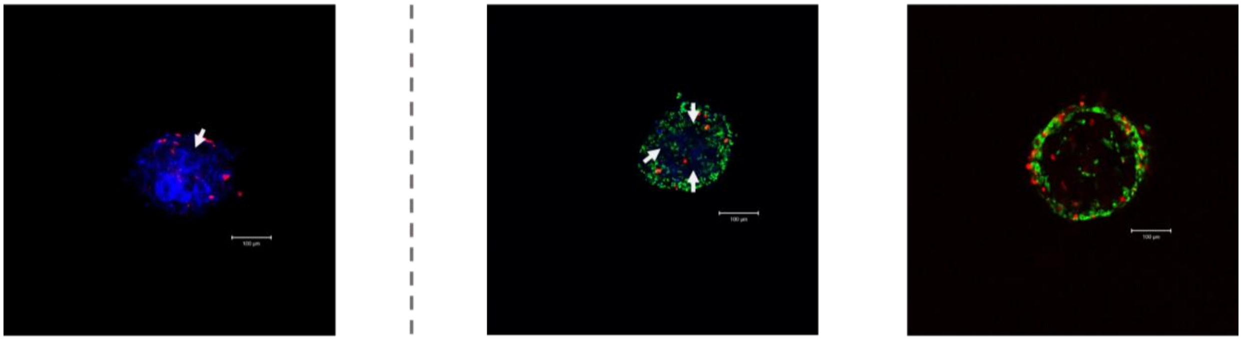

Figure 13. Suppressed aggregation capacity under PML OE. A central confocal slice of one U87MG-PML (left) and two U87MG-PML OE spheroids (right). White arrows represent vacant areas inside the spheroids. It is observed that these areas increase in size and number under PML OE. Blue (H2DCFDA) represents the cell somata, red (DRAQ7) represents the dead nuclei and green (DsRed) represents the PML protein. Scale bar is set at 100um.

LSFM and confocal images in (Figure 14) were captured 72h after spheroid formation. The growth of a U87MG-PML (a&c) and a U87MG-PML OE (b&d) representative spheroid. It is observed that the PML protein is uniformly distributed within the spheroid and the cell death pattern is not considerably affected.

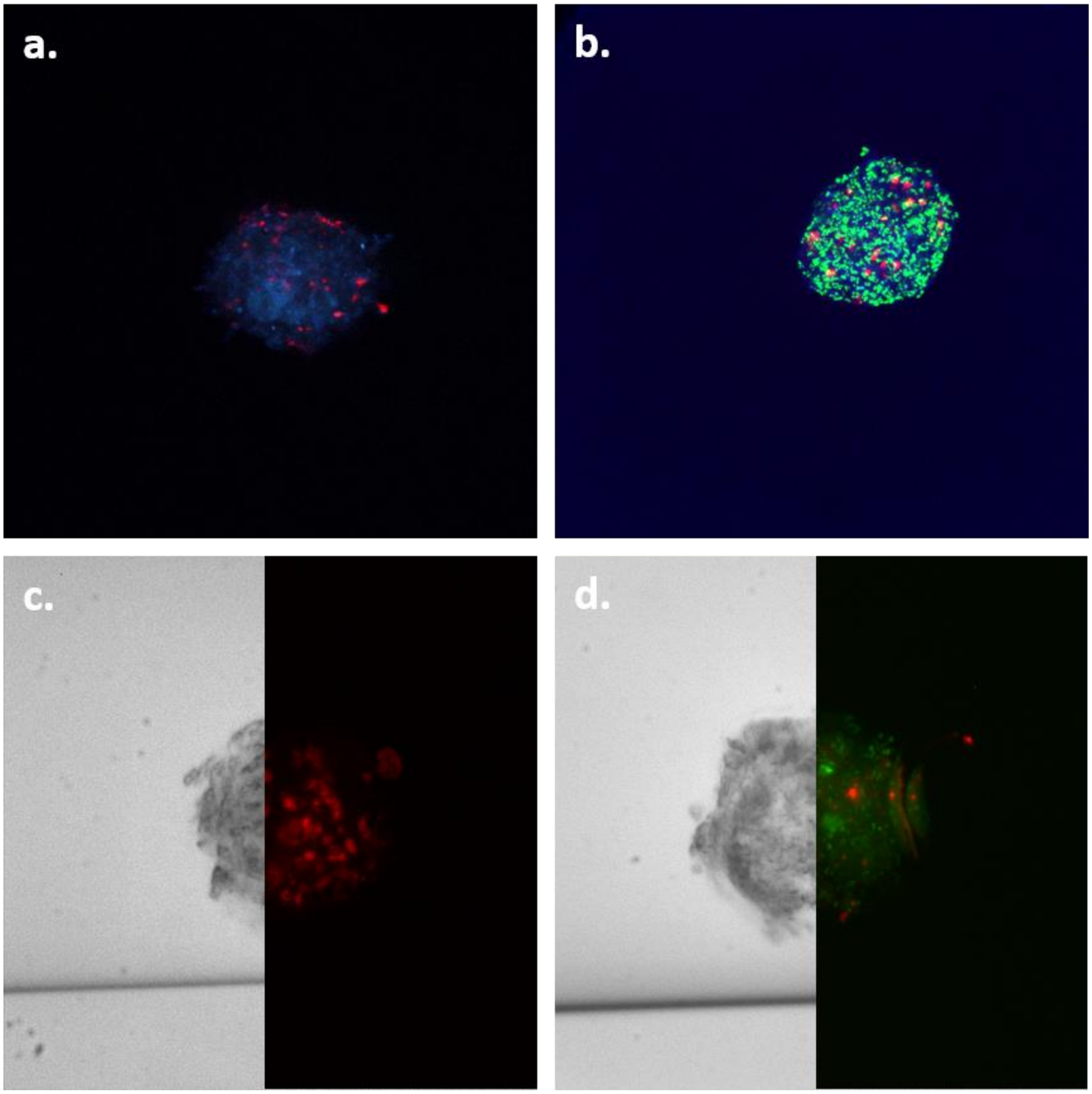

Figure 14. Confocal (a-b) **and LSFM (c-d) scans of the growth expansion of a U87MG-PML** (a&c) **and a U87MG-PML OE** (b&d) **representative spheroid within the μ-slide plate or the FEP-tube respectively 72h after spheroid formation. Dead nuclei are shown in red and live cells are shown in blue. The DsRed/PML distribution is shown in green.**

3.2. TUMOR INVASION

In order to monitor the invasive properties of the U87MG-wt and U87MG-PML/OE spheroids, the invasion process was conditionally allowed by transferring the respective spheroids in an ECM-like substrate environment. Optical microscopy was used every 24h to monitor the invasive pattern of the spheroids of each cell type up to 10 days. The invasive capacity of the spheroids was estimated by both the morphological characterization of the pattern adopted and the dynamics of the invasive rim in means of the radial expansion and the cell density.

In (Figure 15) the invasive morphology all cell lines used is depicted. The bright field images depict the spheroids from the initial until the final time point, while the growth curves represent the radial/areal expansion of the spheroid core, the invasive rim and the total/whole area over time. The U87MG-wt/U87MG-PML cells exhibited the typical starburst invasive morphology (Oraiopoulou et al., 2018). The U87MG-PML OE cells maintained the starburst invasive morphology, yet with altered migration dynamics. Even though, the core of the U87MG-PML OE invasive spheroid was significantly smaller than the U87MG-wt/U87MG-PML, the expansion area of the invasive rim was the same. Interestingly, the core of the U87MG-PML OE spheroid seemed to initially decrease in size and then deform during invasion, losing the discrete core structure that the U87MG-wt cells typically exhibit (Figure 15).

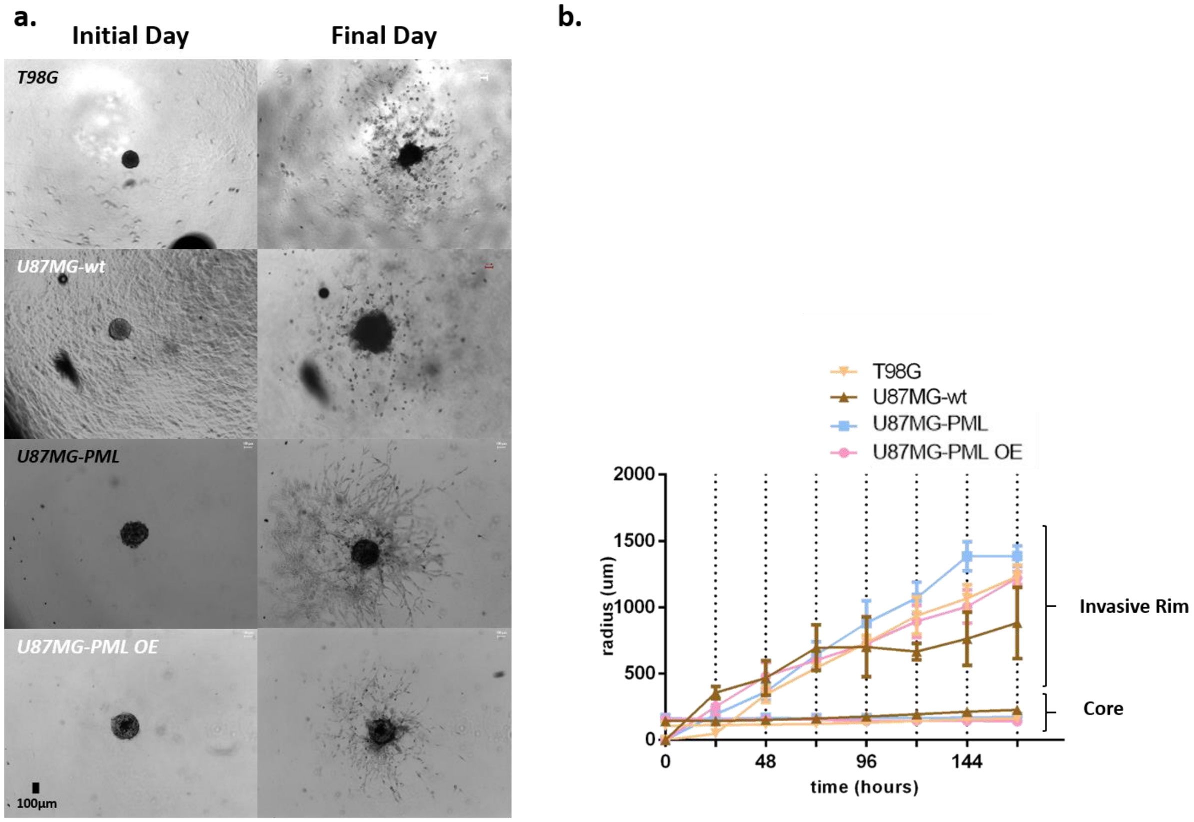

Figure 15. Invasive expansion of the T98G, U87MG-wt, U87MG-PML and the U87MG-PML OE spheroids within the ECM-like substrate environment in the U-bottom plate. (a) **Bright field images of the expansion of the representative spheroids from the initial time point of spheroid formation and seeding within the ECM-like substrate and the final day of the experiment at 216h of the spheroid invasion (initial day left column, final day right column). Scale bar is set at 100 microns.** (b) **Spatiotemporal evolution curves representing the radial expansion of the core and the invasive rim of the spheroids overtime.**

LSFM and confocal images in (Figure 16) were captured at 72h of the spheroid invasion and depict the area expansion of the core and the invasive rim of a U87MG-PML and a U87MG-PML OE spheroid. The invasive pattern of both spheroids exhibited the starburst morphology within the FEP-tube and the μ-slide. The core of the U87MG-PML spheroid was larger in size than the U87MG-PML OE spheroid.

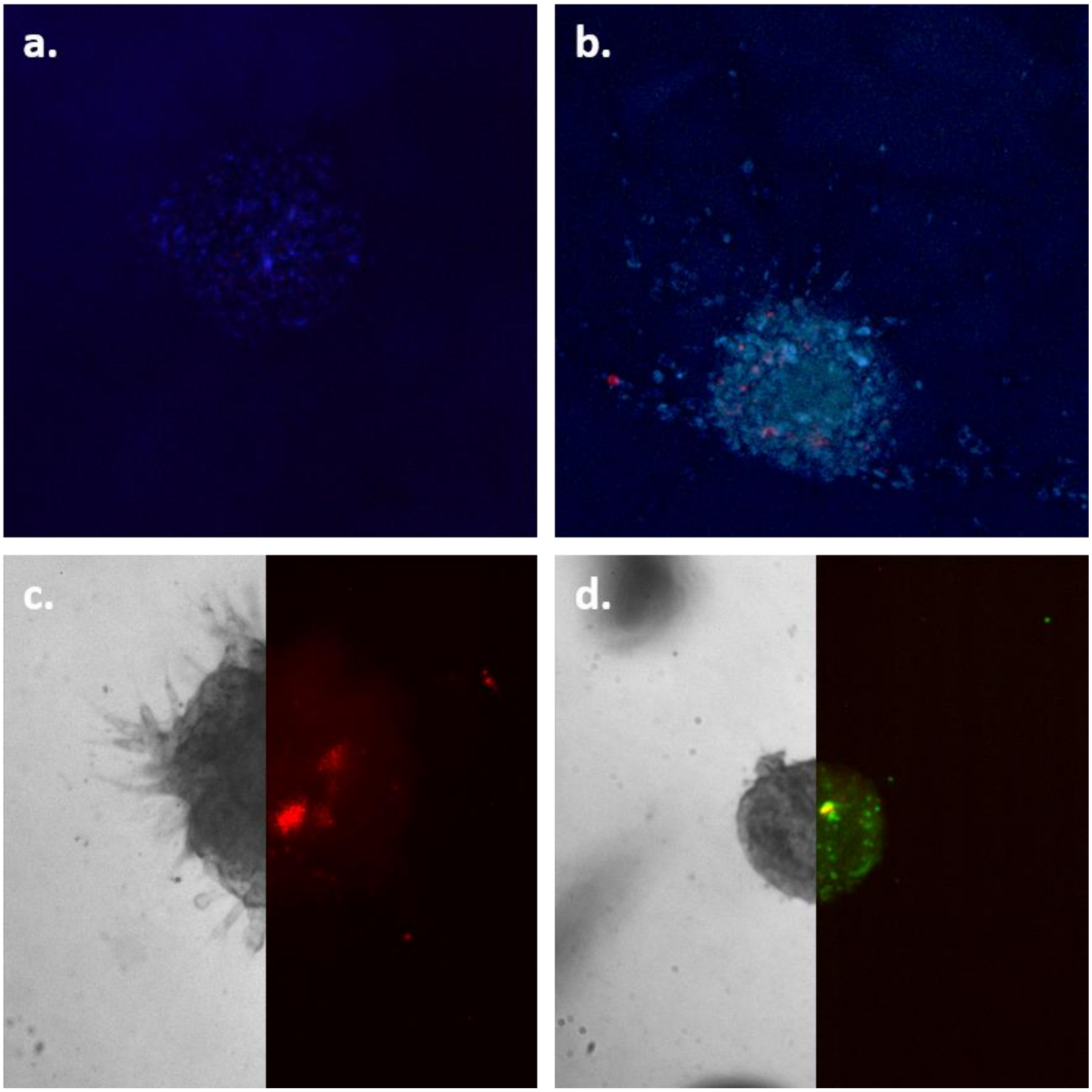

Figure 16. Confocal (a-b) and LSFM (c-d) scans of the invasive expansion of a U87MG-PML (a&c) and a U87MG-PML OE (b&d) representative spheroid within the μ-slide plate or the FEP-tube respectively after 72h. Dead nuclei are shown in red and live cells are shown in blue. The DsRed/PML distribution is shown in green.

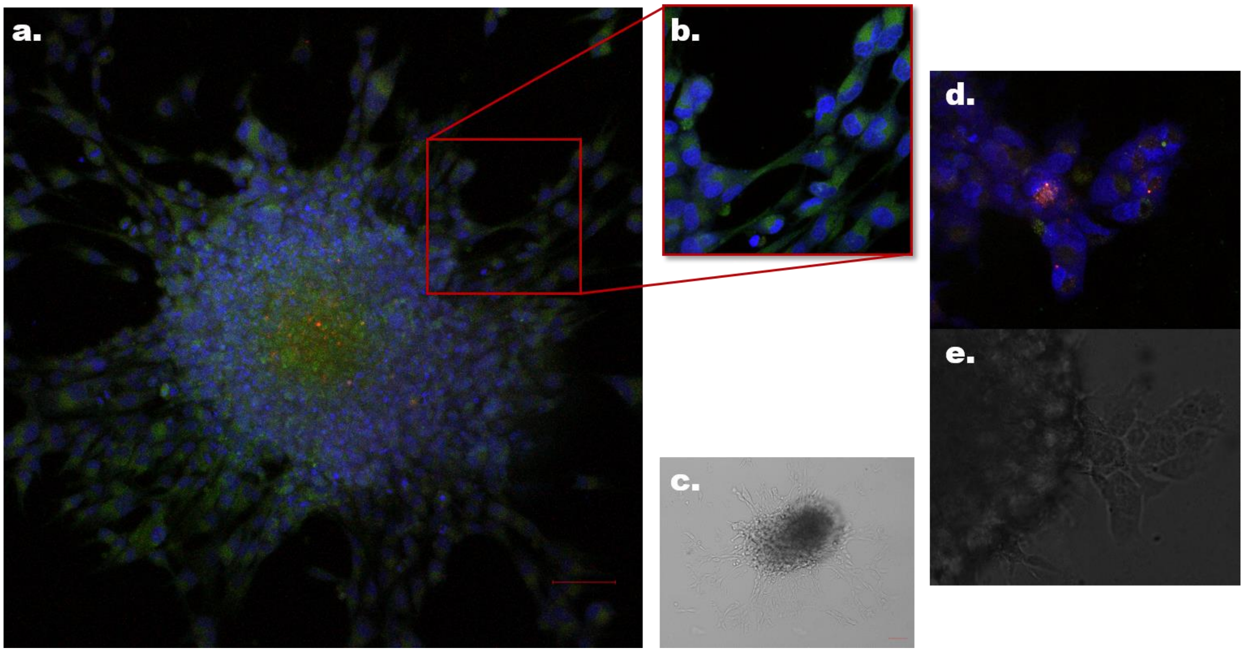

Figure 17. The invasive morphology and physiology adopted by a T98G representative spheroid. (a) Confocal image of a T98G invasive spheroid after 24h. (b) Magnified illustrated invasive region. (c) The brightfield image of the invasive spheroid of image (a). (d-e) An invasive region in both fluorescent and brightfield images. Cells that are in contact appear to have E-cadherin expression at the adhesive spots. High PKH26 (red) signal intensity indicates low proliferative activity. Nuclei are shown in blue. GFP is shown in green. White arrows depict dividing cells. Scale bar is set at 100μm.

3.3. DISSECTING FURTHER THE PML PATHWAY

In order to study further the underlying mechanisms of PML-driven growth and invasive properties, the PML activity was targeted using the drug DZNeP, which disables the EZH2-mediated tumor growth and invasion processes (Girard et al., 2014; Rosa et al., 2016). The U87MG-wt, U87MG-PML and the U87MG-PML OE cell lines were treated with DZNeP in both 2D and 3D conditions. In 2D, the effect of the drug was assessed using the MTT viability assay, whereas in 3D it was estimated by measuring the areal expansion of the spheroid.

In (Figure 18a), the brightfield images depict the growth expansion of the non-invasive spheroids under drug treatment at 3 timepoints. Top row depicts the control spheroids, which were treated with DMSO. Bottom row depicts the spheroids treated with DZNeP at of 30uM, at which approximately 100% of growth inhibition is reached. The growth inhibition curves (Figure 18b) depict the effect of DZNeP on growth expansion overtime. It is observed that there are no significant differences between the treated U87MG-PML and U87MG-PML OE spheroids independently.

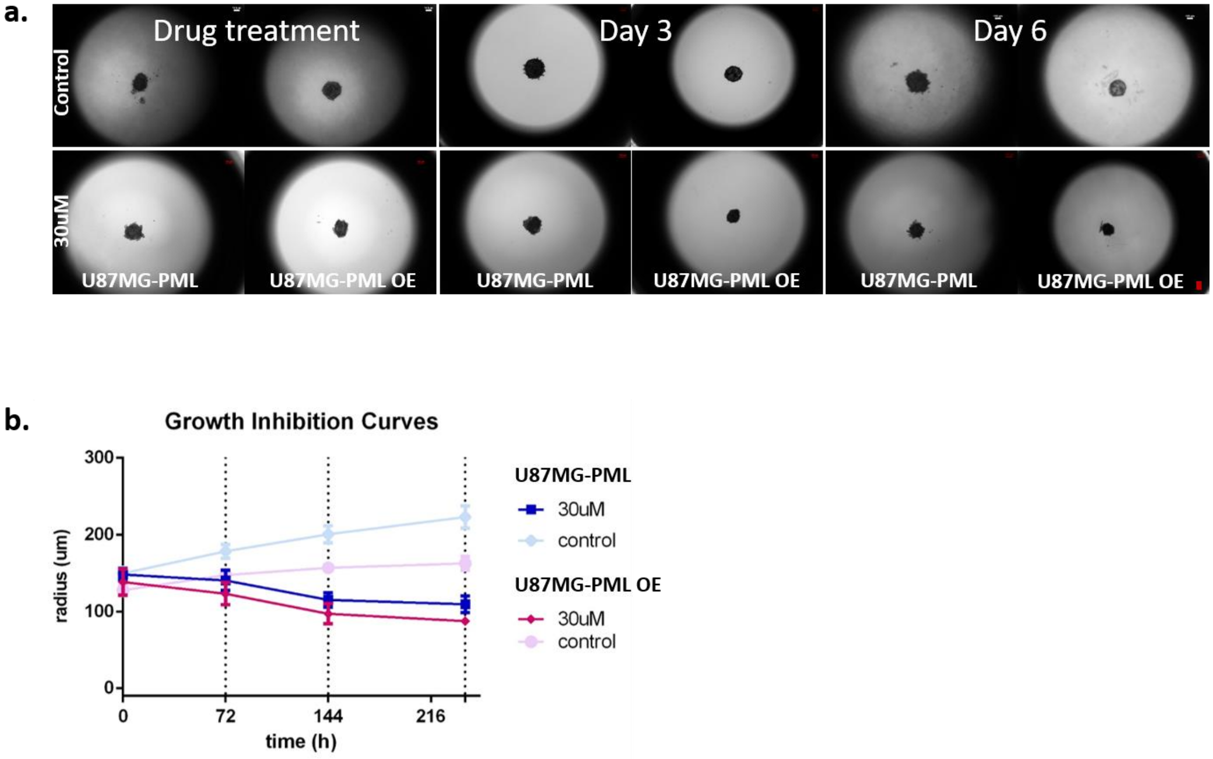

Figure 18. Growth inhibition for the U87MG-PM and U87MG-PML OE spheroids after DZNeP treatment. (a) **Brightfield captions of the growth expansion of the non-invasive spheroids under drug treatment at 3 time points. Control spheroids (top row) were treated with DMSO 1nM. Treated spheroids (bottom row) were treated with 30uM DZNeP. Scale bar represents 100um.** (b)**The growth expansion curves depict the spatiotemporal growth inhibition over time.**

In Figure 19, the brightfield images and the growth curves depict the radial expansion of the core and the invasive rim of the invasive spheroids under drug treatment. It is observed that even though the core of both U87MG-PML and U87MG-PML OE spheroids is not significantly affected, the invasive rim is reduced compared to the untreated controls for both cell lines. In particular, the invasive rim of the U87MG-PML OE cells was almost eliminated after treatment with the highest concentration, indicating that the targeted pathway is essential for the regulation of invasion in U87MG-PML OE cells.

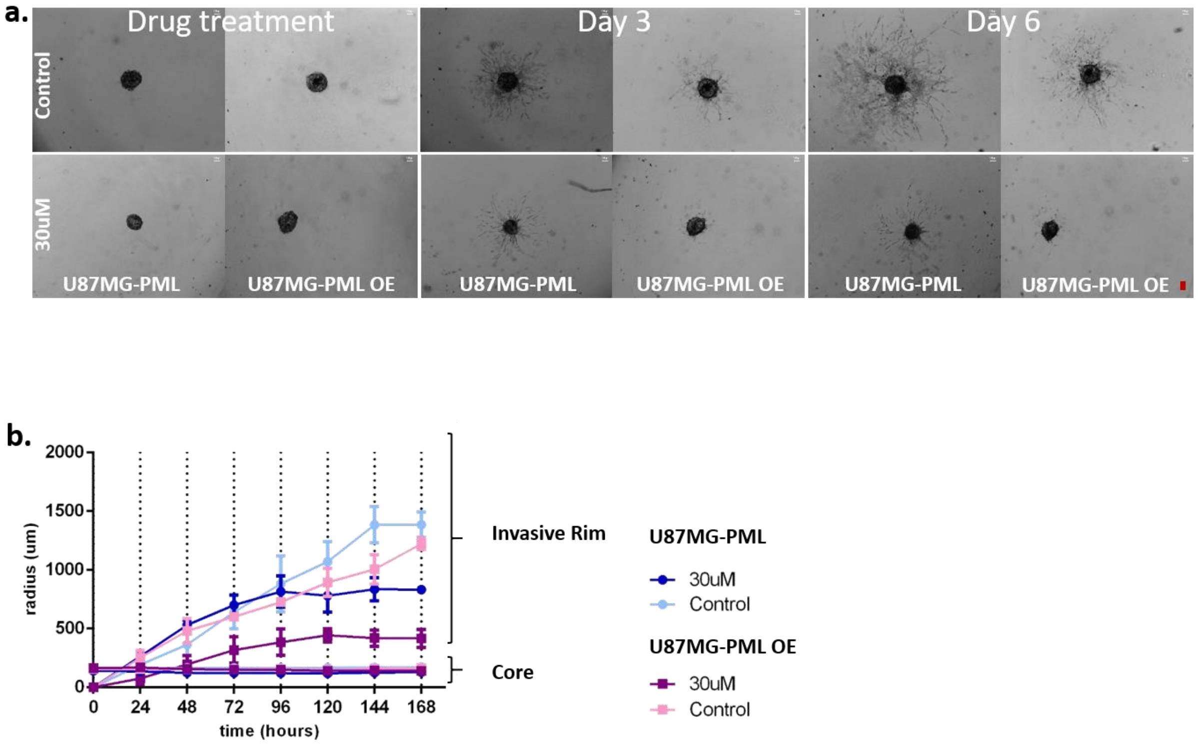

Figure 19. The invasion dynamics of the U87MG-PML and U87MG-PML OE spheroids under DZNeP treatment overtime. (a) Brightfield captions of the invasive expansion of the invasive spheroids under drug treatment at 3 time points. Control spheroids (top row) were treated with DMSO 1nM. Treated spheroids (bottom row) were treated with 30uM DZNeP. Scale bar represents 100um. (b)**The invasion curves depict the spatiotemporal growth and invasive inhibition over time**

Confocal images of the invasive and the non-invasive representative spheroids treated with DZNeP at highest concentration were captured 72h after treatment (Figure 20 & Figure 21). The dead nuclei are shown in red and the live cells are shown in blue. The DsRed/PML distribution is shown in green. As expected, the cell death pattern is similar between the U87MG-PML and U87MG-PML OE spheroids. However, the U87MG-PML OE spheroids showed a significant reduction of the invasive rim.

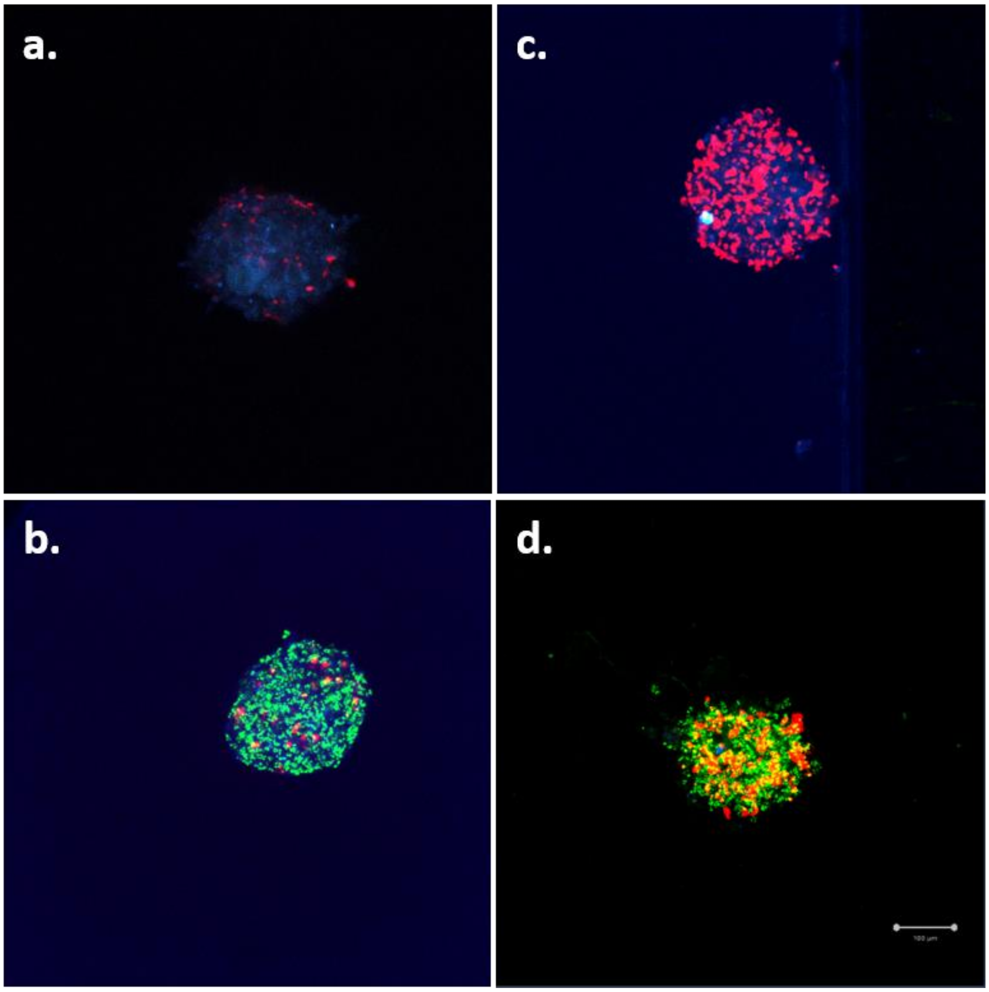

Figure 20. Confocal images of the non-invasive U87MG-PML and U87MG-PML OE representative spheroids, 72h after DZNeP treatment. (a & c) **depict the U87MG-PML and (b & d) depict the U87MG-PML OE.** (a & b) **show the control-untreated spheroids, while** (c & d) **show the spheroids treated with DZNeP at highest concentration (30uM). Dead nuclei are shown in red and live cells are shown in blue. The DsRed/PML distribution is shown in green. Scale bar is set at 100um.**

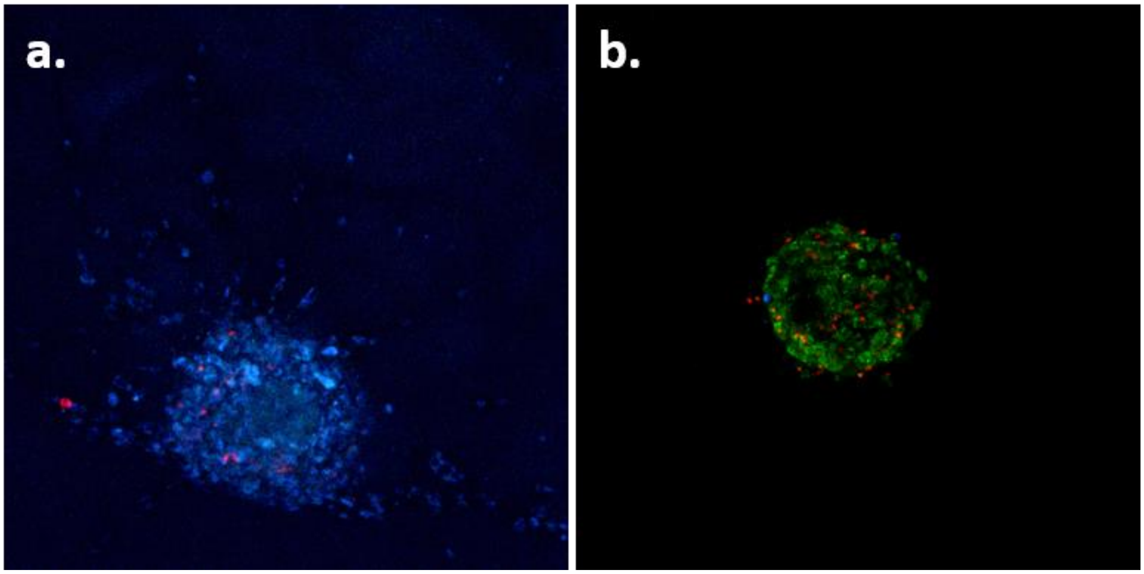

Figure 21. Confocal images of the invasive U87MG-PML OE representative spheroids, 72h after DZNeP treatment. (a) **The control/untreated U87MG-PML OE spheroid.** (b)**The spheroid treated with DZNeP at highest concentration (30uM). Dead nuclei are shown in red and live cells are shown in blue. The DsRed/PML distribution is shown in green.**

3.4. *IN SILICO* SIMULATIONS

In order to further study our hypothesis, we used *in silico* modeling to simulate the tumor evolution. We silenced the EZH2-mediated pathways in order to highlight the PML-mediated direct effects and isolate the two distinct physiological phenomena.

3.4.a. INITIALIZING THE COMPUTATIONAL MODEL TO STUDY THE EFFECT OF THE PARAMETERS

A parameter study is conducted to investigate the extent at which each parameter affects tumor evolution. The physiology of the non-invasive spheroids is first investigated and the non-induced (U87MG-PML) *in vitro* estimations are used as a reference value. The parameters explored in the non-invasive condition include the proliferation time, random cell death, proliferation depth, and initial cell density (Figure 22). We observed that by increasing the proliferation time of the cells, they become slower, therefore the growth expansion is negatively affected (Figure 22a). On the other hand, an increase of the proliferative depth results in less contact inhibition, thus higher expansion (Figure 22b). As expected, increasing the random cell death probability the growth expansion is reduced (Figure 22c). Furthermore, reducing the cellularity of the initial spheroid, the number of the cells composing the tumor is reduced, therefore the tumor expansion is slower

(Figure 22d). Once the effect is observed, the values that better fit and describe the *in vitro* experiments are determined.

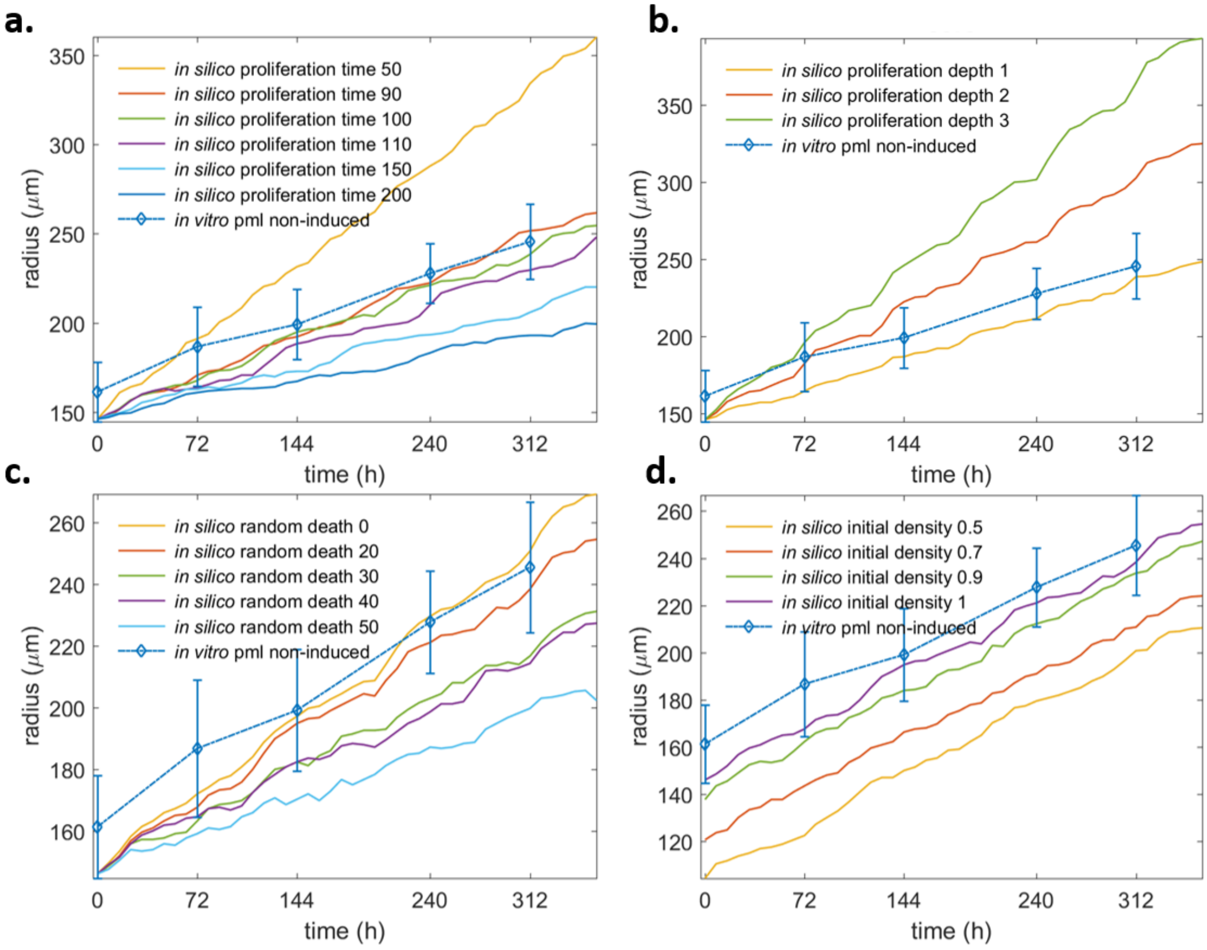

Figure 22. Parameter study regarding the growth properties of the U87MG cells. U87MG-PML *in vitro* estimates are used as reference. Parameter study investigating the role of (a) proliferation time, (b) proliferation depth, (c) random death rate and (d) initial cell density.

A same study is performed regarding the invasive spheroids and the U87MG-PML *in vitro* estimations are again used as reference values. The parameters studied in the invasive condition are the diffusion coefficient of the cells and the phenotypic ratio (Figure 23). Because diffusion is a random process and the *in silico* tumor is composed of few tumor cells, all the experiments have been repeated 10 times. The mean and standard deviation of the core and invasive rim estimates as shown in (Figure 23) has been derived from all the experiments performed. It is observed that the diffusion coefficient does not affect the core dynamics (Figure 23a). Yet, it significantly affects the dynamics of the invasive rim in a positive way. As the diffusion coefficient increases, the expansion of the invasive rim is higher (Figure 23b).

For the phenotypic ratio, it is assumed that that the tumor is composed of cells with different phenotypic traits with respect to the adhesion property. In particular, we assume that the U87MG spheroids are composed of phenotypes with very high cell-to-cell adhesiveness (Adhesive) and very low adhesiveness (Motile). The ratios shown reflect the initial Motile:Adhesive ratio. In the parameter study it is observed that increasing the ratio of Motile phenotypes relative to Adhesive, while keeping the diffusion coefficient the same, a profound decrease in the core dynamics and a significant increase in the invasive rim expansion are observed (Figure 23c-d)

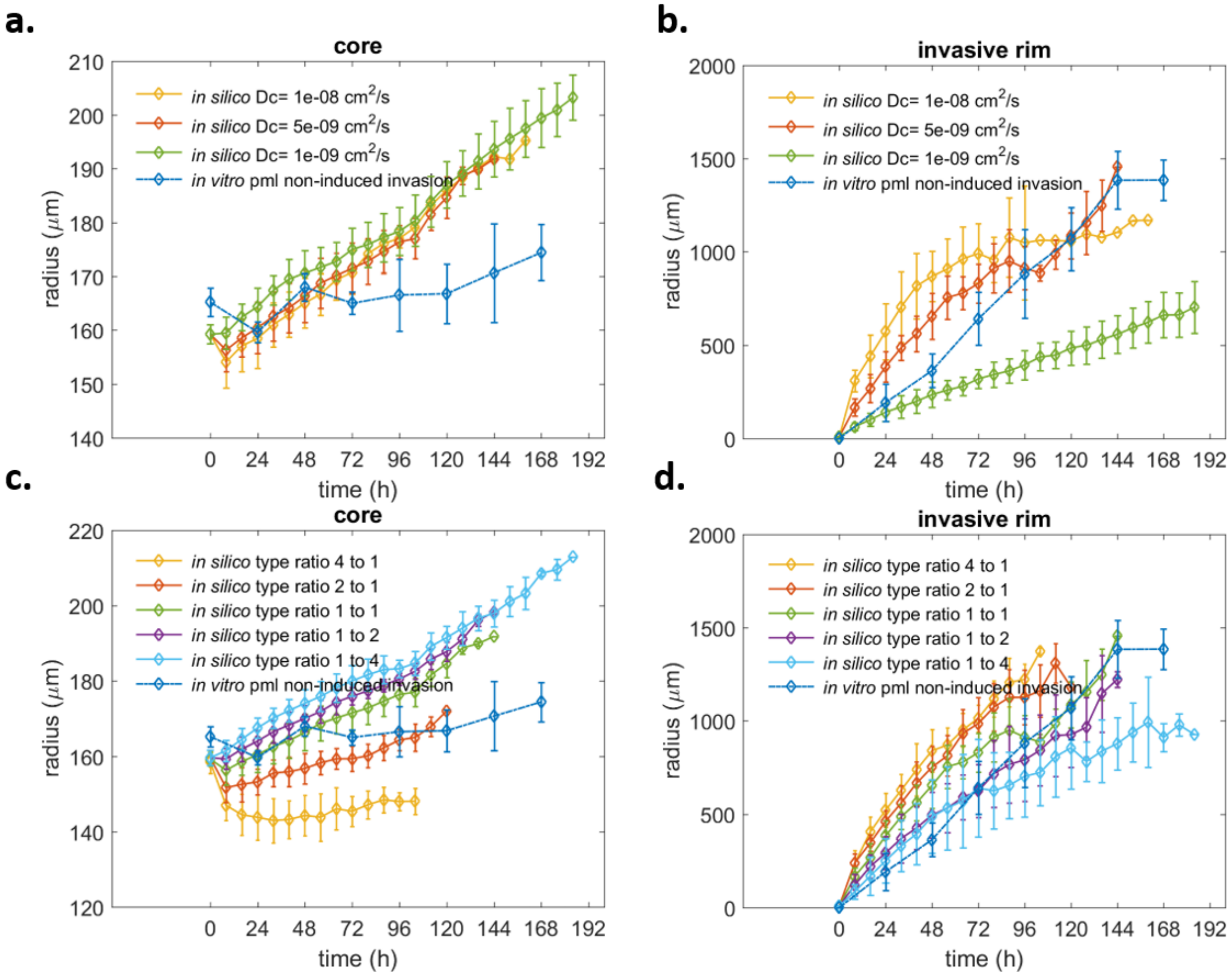

Figure 23. Parameter study regarding the invasive dynamics of the U87MG cells. . U87MG-PML *in vitro* estimates are used as reference. Parameter study investigating the role of (a-b) diffusion coefficient, (c-d) and seeding population ratio regarding the adhesive phenotypes.

3.4.b. COMPARISON OF BIOLOGICAL AND COMPUTATIONAL RESULTS

3.4.b.i. TUMOR GROWTH STUDY

Based on the biological observations and the thorough parameter study of the modeling parameters that was performed, the parameters that best fit the growth dynamics of the U87MG-PML *in vitro* spheroids in the non-invasive condition were selected. Keeping all the rest parameters fixed, variation in the proliferation time was allowed, in order to describe and quantify the altered growth dynamics observed in the U87MG-PML OE cells. The simulations showed that a 60% increase of the proliferation time in the U87MG-PML OE cells relative to the U87MG-PML cells can well-explain the growth curve of the U87MG-PML OE spheroids in accordance to the doubling time experiments (Figure 24). We then investigated the (30uM) DZNeP-mediated death on the growth dynamics. We concluded that a death rate equal to 0.0065h-1, which corresponds to 65% of the proliferation rate of the U87MG-PML cells can explain the growth inhibition observed in both the U87MG-PML (Figure 25a) and the U87MG-PML OE (Figure 25b) spheroids under (30uM) DZNeP treatment. Note that for the case of the U87MG-PML OE spheroids, this death rate is approximately equal to their proliferation rate, resulting in their significant growth inhibition and increased overall death.

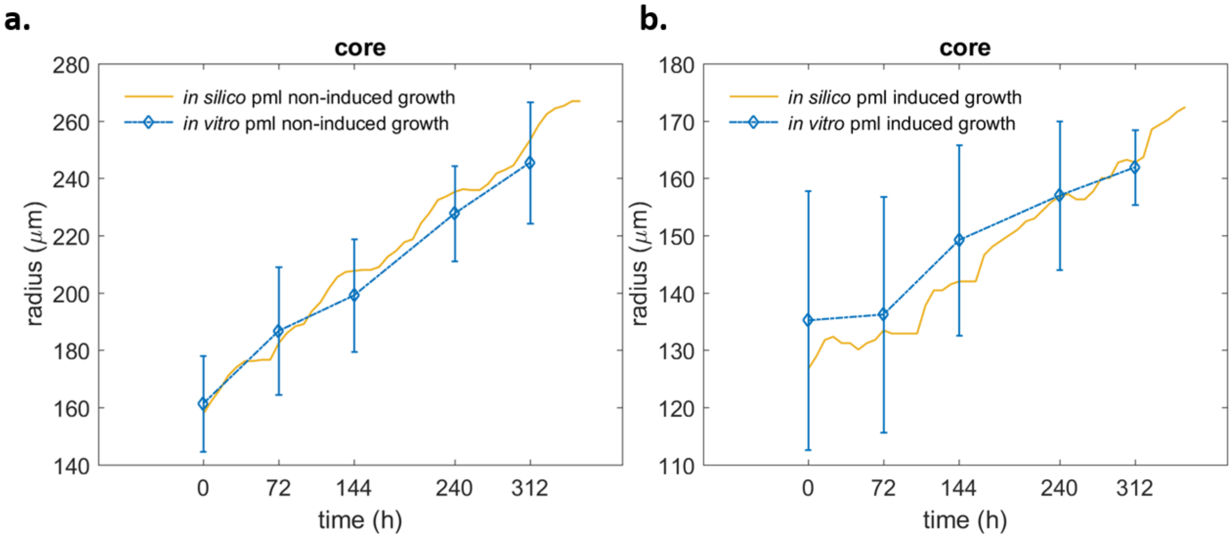

Figure 24. Growth dynamics in the non-invasive condition. (a) U87MG-PML and (b) U87MG-PML OE spheroids overtime. The in vitro estimates are also shown for comparison.

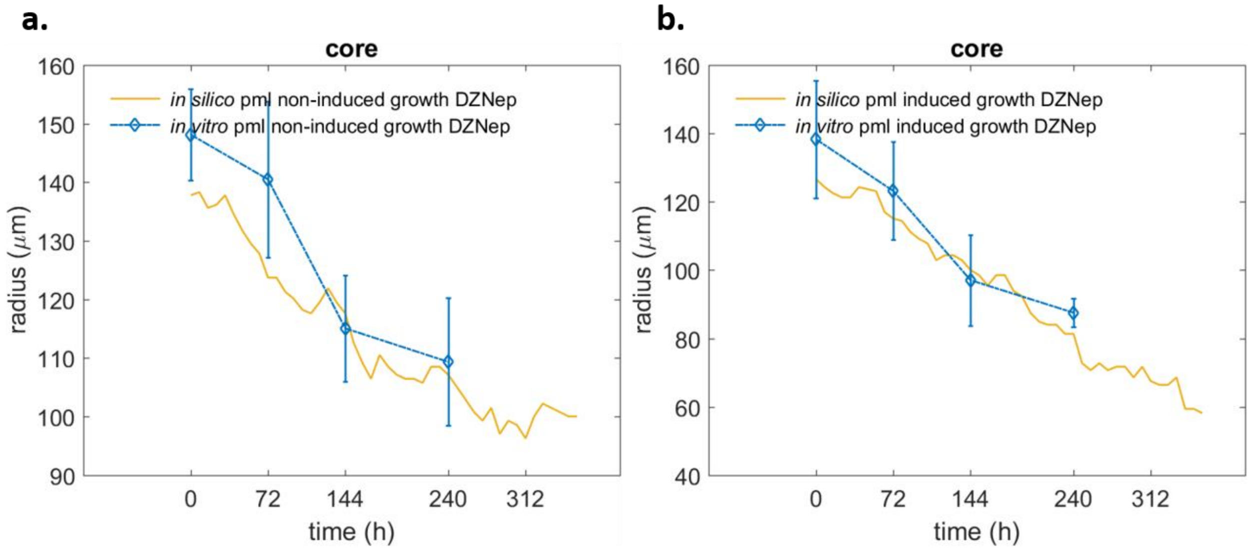

Figure 25. Growth dynamics in the non-invasive condition. (a) U87MG-PML and (b) U87MG-PML OE spheroids overtime under DZNeP (30uM) treatment. The in vitro estimates are also shown for comparison.

3.4.b.ii. TUMOR INVASION STUDY

In order to mathematically describe the invasive capability of both the U87MG-PML and U87MG-PML OE spheroids, it is assumed that the tumor is composed of cells with different phenotypic traits (Motile and Adhesive). Thus, the invasive pattern exhibited in the simulations was attributed in probabilistic cell movement of different subpopulations regarding their cell-to-cell adhesion properties. Note that adhesive property of the cells does not affect the growth dynamics of the proliferative conditions; it only affects the expansion dynamics in the invasive conditions. The simulations showed that an initial ratio of Motile:Adhesive approximately equal to 2:1 well-describes the expansion dynamics of the core and the invasive rim of both the U87MG-PML (Figure 26) and U87MG-PML OE (Figure 27) spheroids.

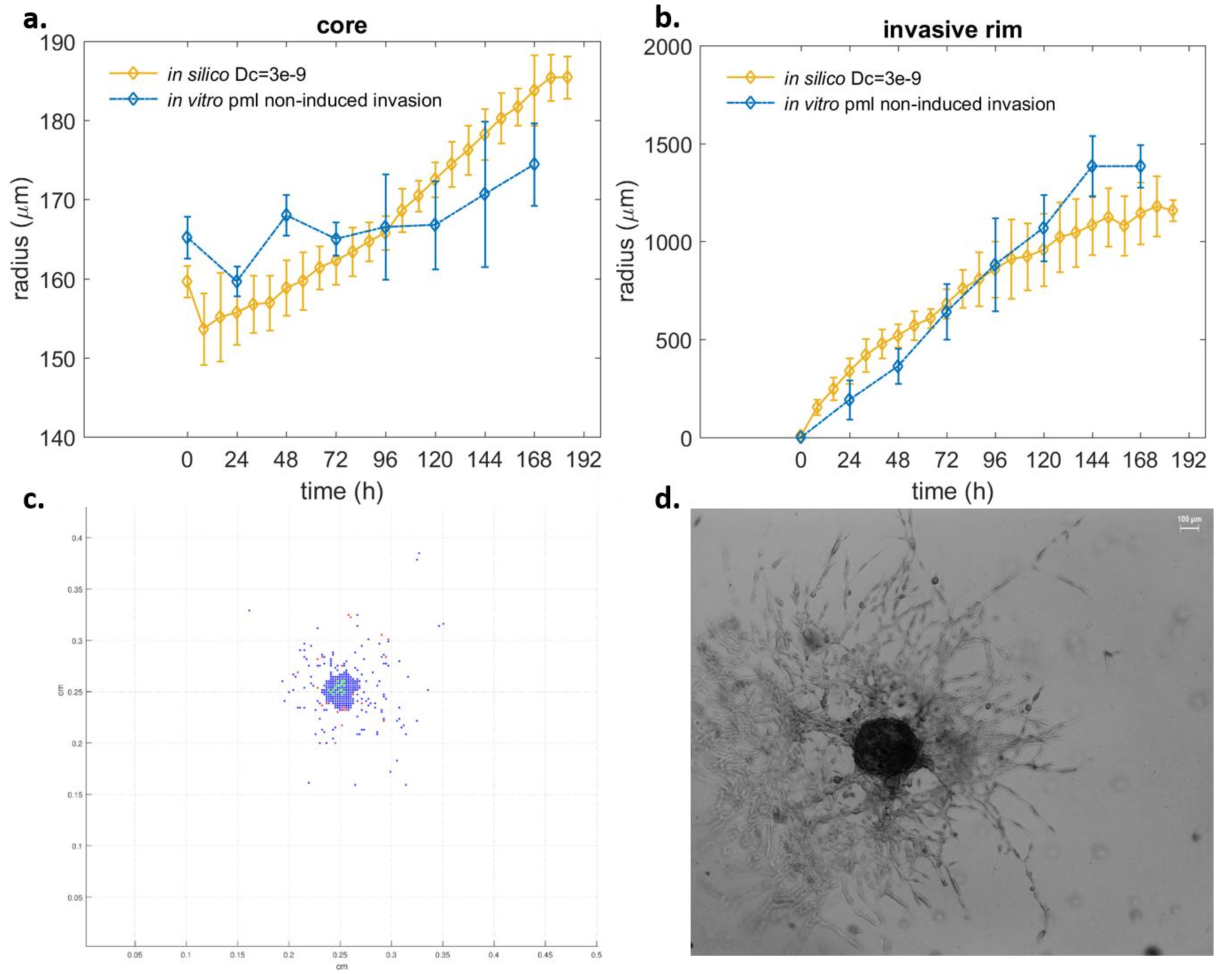

Figure 26. Invasive dynamics of the U87MG-PML spheroids. (a) core and (b) invasive rim expansion over time. The *in vitro* estimates are also shown for comparison. (c) *in silico* snapshot and (d) brightfield image of a representative U87MG-PML spheroid at t=144h.

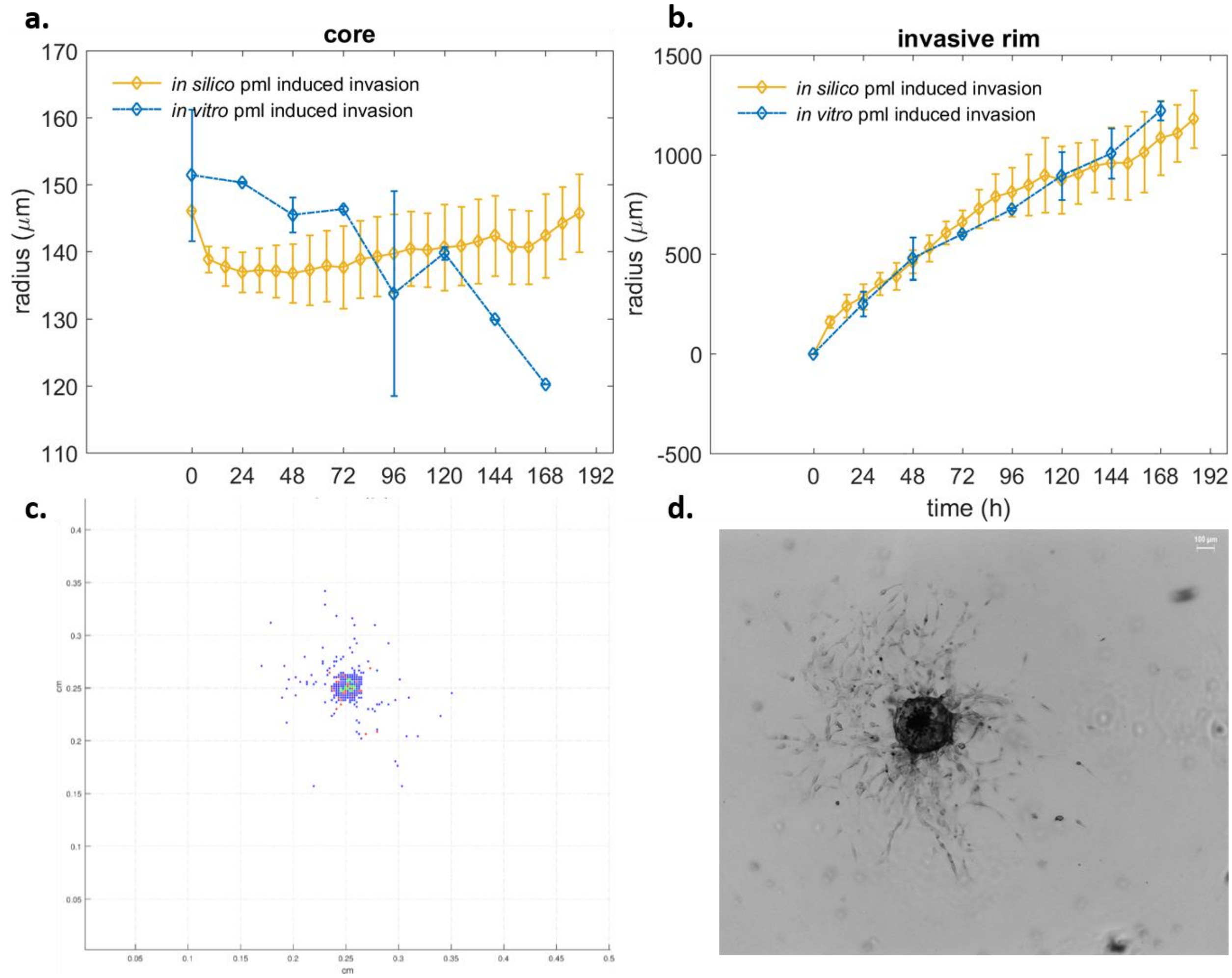

Figure 27. Invasive dynamics of the U87MG-PML OE spheroids. (a) core and (b) invasive rim expansion over time. The *in vitro* estimates are also shown for comparison. (c) *in silico* snapshot and (d) brightfield image of a representative U87MG-PML OE spheroid at t=144h.

Furthermore, in both cell lines, the Diffusion coefficient of the random movement equals to 3e-9 cm2/s. Note that in all the invasion experiments, the proliferation rate, as well as the other parameters used to best fit the U87MG-PML and the U87MG-PML OE spheroids in the non-invasive condition have been kept correspondingly the same. The presence of DZNeP in the invasive conditions has been assumed to act with the same death rate as in the non-invasive conditions. Here, we investigate its potential role on motility speed as reflected in the Diffusion coefficient and Motile:Adhesive ratio. It is observed that in the presence of DZNeP, variations in the motility speed cannot capture both the core and the invasive rim dynamics. Interestingly, we observed that the dynamics of the treated U87MG-PML are well-approximated when the Motile:Adhesive ratio changes from 2:1 to 1:1 (Figure 28). We also showed that in order to explain the motility inhibition observed in the U87MG-PML OE cells under DZNeP treatment, the alternative initialization as regards the ratios of the motile and the adhesive phenotypes was the critical parameter in order to reach the different dynamics of both the invasive rim and core spheroid. In particular, further reduction relative to the U87MG-PML of the initial motile phenotypes to 1:2 was necessary (Figure 29). In other words, DZNeP presence was shown to eliminate the motile phenotypes in the PML overexpression condition. Especially for the U87MG-PML OE treated spheroids, note that in the invasive rim the motile cells are relatively less and most of them are dead, as it can also be observed in the respective figure of the optical microscope.

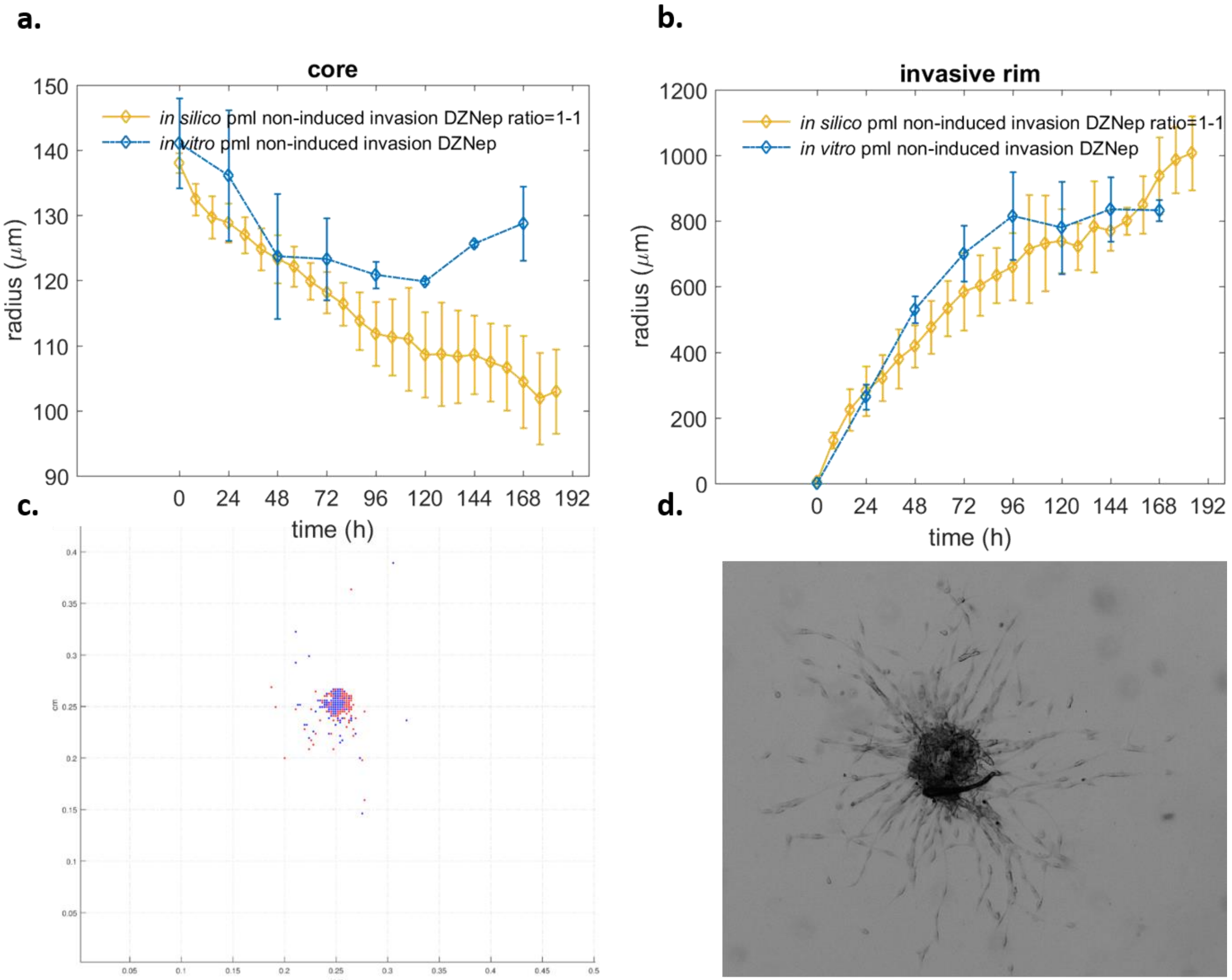

Figure 28. Invasive dynamics of the U87MG-PML spheroids under DZNeP treatment. (a) core and (b) invasive rim expansion over time. The in vitro estimates are also shown for comparison. (c) in silico snapshot and (d) brightfield image of a representative U87MG-PML spheroid under DZNeP treatment.

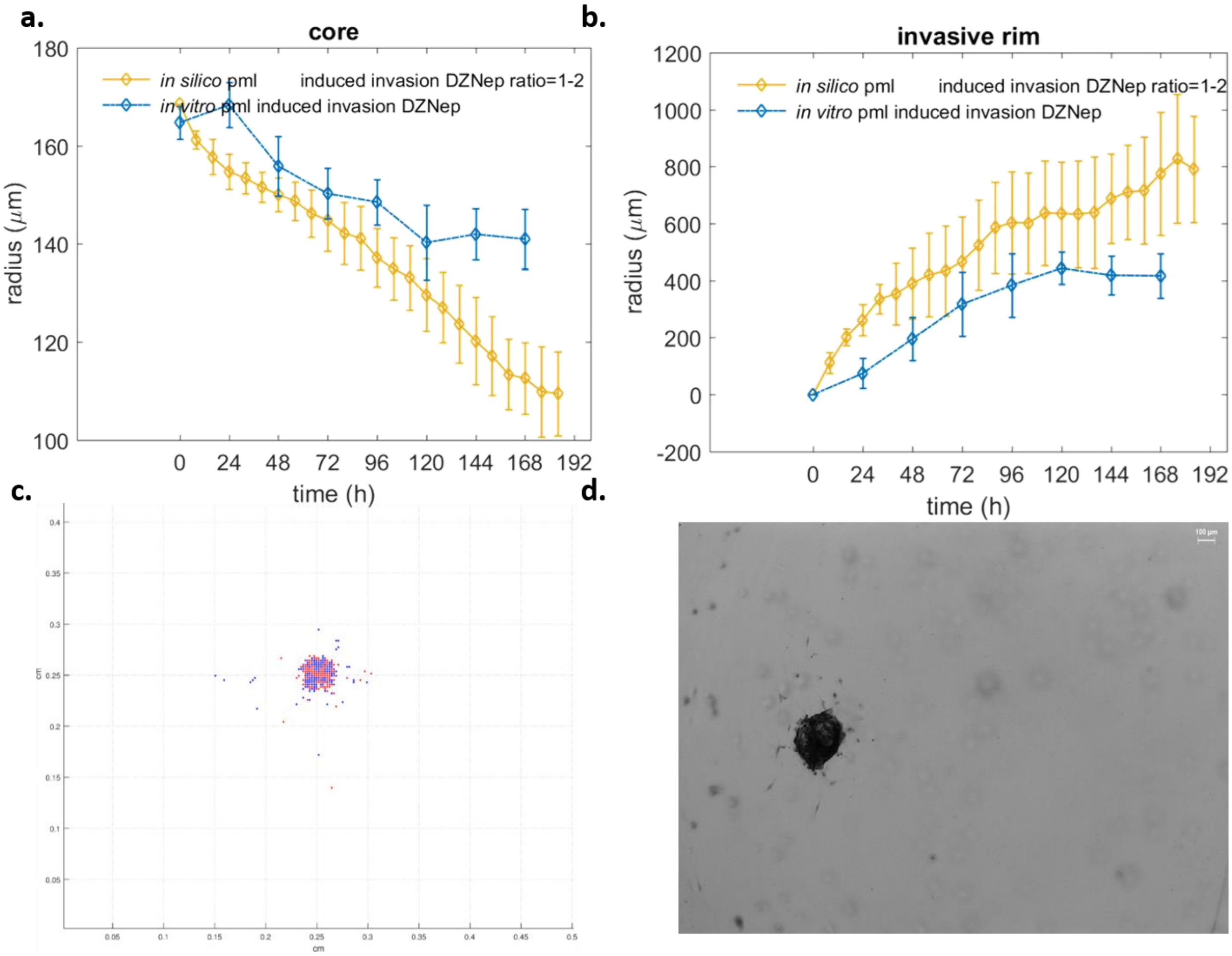

Figure 29. Invasive dynamics of the U87MG-PML OE spheroids under DZNeP treatment. (a) core and (b) invasive rim expansion over time. The in vitro estimates are also shown for comparison. (c) in silico snapshot and (d) brightfield image of a representative U87MG-PML OE spheroid under DZNeP treatment.

4. DISCUSSION

In this work the physiological role of the PML protein in GB secondary cell cultures is investigated. For this purpose, 2D and 3D biological models have been applied, imaged with optical and fluorescence microscopy and modeled with computational predictive algorithms. In this way, an *in vitro-in silico* approach is performed, in order to better understand and quantify the effect of PML-mediated mechanisms on GB proliferation and invasion. The invasive capacity of the T98G (ATCC® CRL-1690TM, USA) and the well-established GB cells U87MG (ATCC® HTB-14™) was investigated. Followingly, the U87MG cells were used to own-establish the U87MG-PML cell line and the U87MG-wt and T98G cell lines were used as control. The physiology of all cell types was observed using conventional optical, LSFM and confocal microscopy and the specific phenotypes were translated into computational parameters in a custom-made CA individual-cell-based predictive model.

PML OE inhibits cell aggregation and spheroid formation. The U87MG-PML OE cells exhibited reduced aggregation capacity. They generated smaller and occasionally deformed spheroids (Figure 12) in conventional media, and typically needed a longer time interval for the spheroid formation compared to the controls. Even though, the T98G control cell line also exhibited low aggregation dynamics, they formed the spheroids at the same time point with the U87MG-wt cells. We also tested whether the aggregation dynamics of the U87MG-PML OE cells would be affected under varying concentrations of FBS (data not shown). As it has been previously observed, media additives can alter the aggregation capacity in 3D/hanging-drop cell cultures (Leung et al., 2015). However, no change in sphere-forming was observed in the U87MG-PML OE cells. The only condition that spheroid formation was facilitated, was under the addition of an ECM-like substrate within the hanging drop, which has been previously suggested to improve cellular aggregation and formation of 3D structures (Foty, 2011; Leung et al., 2015). All these findings are is in line with previous reports, indicating that PML IV reduces cell aggregation and sphere formation due to its inhibitory effect on the cancer stem cells and their self-renewal capacity (Sachini et al., 2019).

PML OE induces tumor growth inhibition. The U87MG-PML OE cells exhibited increased proliferation time compared to the controls in the doubling time/trypan blue viability assay experiments. Furthermore, as also shown in previous reports (Amodeo et al., 2017), PML OE reduced the tumor growth expansion of the 3D spheroids, also indicating lower proliferative capacity. The proliferation time of the cells can be attributed to a variety of factors affecting their growth properties. The spontaneous/intrinsic cell death rate, for example is a key characteristic of each cell line and contributes to the progression of the tumor. The PML IV isoform is a regulator of apoptosis, senescence and DNA damage by the p53 protein activation (Nisole et al., 2013). Yet, the trypan blue viability assay, as well as the LSFM and confocal imaging, revealed no significant differences in the spontaneous cell death rates for the U87MG-PML OE cells and the controls, indicating that the proliferation time prolongation is not attributed to an increased cell death pattern. FACS analysis for cell-cycle exhibited an increased S-phase fraction, followed by a decreased G2/M-phase, suggesting that the growth inhibition could be attributed to a cell-cycle arrest. Our results are in line with previous findings, indicating that PML OE results in decreased proliferation rate and cell-cycle restriction (Iwanami et al., 2013; Sachini et al., 2019). These studies propose the cell-cycle arrest in the G0/G1 fraction, however they refer to different PML isoforms or biological cancer models.

PML affects tumor cell migration. Furthermore, PML OE altered the invasive properties of the U87MG-PML OE cells. The invasive pattern was common in both cell lines adopting the typical starburst morphology (Oraiopoulou et al., 2018), however, they presented different migration dynamics in terms of both the expansion and the cellular density of the invasive rim. Even though, the core of the U87MG-PML OE spheroid was smaller and deformed over time, the border of the invasive rim was eventually the same compared to the U87MG-PML spheroid. The U87MG-PML OE cells formed more dendritic invasive branches near the core and the tumor core exhibited a slight reduction in size during the first invasive time points. This slight reduction is possibly attributed to a higher migratory and a lower proliferative capacity of the U87MG-PML OE cells. **These findings indicate that upon PML presence, tumor growth and migration appear to have antagonistic roles. PML exhibits a pro-migratory behavior and PML OE cells seem to prefer to migrate rather than proliferate.** Our results are in line with previous findings that set PML a regulator of both growth, inducing growth inhibition (Iwanami et al., 2013; Amodeo et al., 2017), and migration via a pro-angiogenic molecule EZH2 (Smits et al., 2011; Amodeo et al., 2017).

Especially in the µ-slide plate, the U87MG-PML OE spheroids exhibited very early and high migratory capacity compared to the U87MG-PML spheroids. However, the total invasive progress of the U87MG-PML and U87MG-PML OE spheroids within the FEP-tube was decelerated, when compared to the invasive spheroids of the same age in the U-bottom or the µ-slide plates. This could be attributed to the changed environmental conditions and it is assumed that both spheroids would eventually exhibit the same respective invasive behavior in the LSFM-tube as they did in the U-bottom plate over time.

PML mediates tumor growth and cellular migration through distinct cellular mechanisms. It has been proposed that PML mediates tumor growth and migration via a PML/Slit Axis (Amodeo et al., 2017). Tumor growth inhibition is regulated by two different pathways, one EZH2 mediated and one non-EZH2 mediated. Tumor migration is also mediated by the PML-EZH2 pathway. Dissecting further the PML mediated pathways, we tested the sensitivity of the U87MG-PML and U87MG-PML OE cells to DZNeP, an EZH2 histone methyltransferase inhibitor. Upon EZH2 inhibition, no difference would be observed regarding the tumor growth properties of the U87MG-PML OE and control cells, independently of the DZNeP dose concentration.

Our results showed no differences between the U87MG-PML and U87MG-PML OE non-invasive spheroids independently of the DZNeP dose concentration, indicating that **the PML induced growth inhibition is mainly mediated by the PML-direct growth inhibitory pathway**. The mathematical model supports and quantifies this hypothesis. When the DZNeP sensitivity was assessed in the U87MG-PML and U87MG-PML OE invasive spheroids, a significant reduction was shown in the invasive rim of the U87MG-PML OE spheroids. This finding indicates that **the EZH2-mediated indirect pathway is highly functional for the PML-mediated cell migration regulation**. **Our findings indicate that in GB, PML inhibits tumor growth while it induces cellular migration and these two PML-driven functions are mediated by distinct cellular mechanisms**.

Interestingly, even, though the DZNeP mediated effects did not vary significantly between the U87MG-PML and U87MG-PML OE cells, the cell death pattern topology was altered. The dead cells were equally distributed within the U87MG-PML spheroid, whereas they were more peripherally detected in the case of the U87MG-PML OE one. We observed that the PML-NBs would decompose late within the apoptotic nucleus, indicating a potential PML relation with this cell death topology differentiation, combined with the known PML IV apoptotic function

***In silico* simulations support the biological hypothesis.** Overall, the parameter study verifies the role of specific physiological parameters in tumor expansion and quantifies the *in vitro* observations. Even though, the employed algorithms describe a cancer predictive model that simulates tumor physiology and cellular phenomena (Oraiopoulou et al., 2017, 2018), in this work, the model was further used to simulate molecular events. The growth and invasive characteristics are intrinsic properties of the cells, not easily isolated in the *in vitro* experiments (see Figure 30 for a simpler adopted version of Figure 4 where our hypothesis is assumed). Therefore, the mathematical model is utilized to discriminate and isolate the biological phenomena, in order to study the specific effects of the PML protein in each condition. The biological experiments initialize the mathematical model and constraining the *in silico* tumor evolution to the initial *in vitro* conditions, the observed physiology is in line with the biological findings.

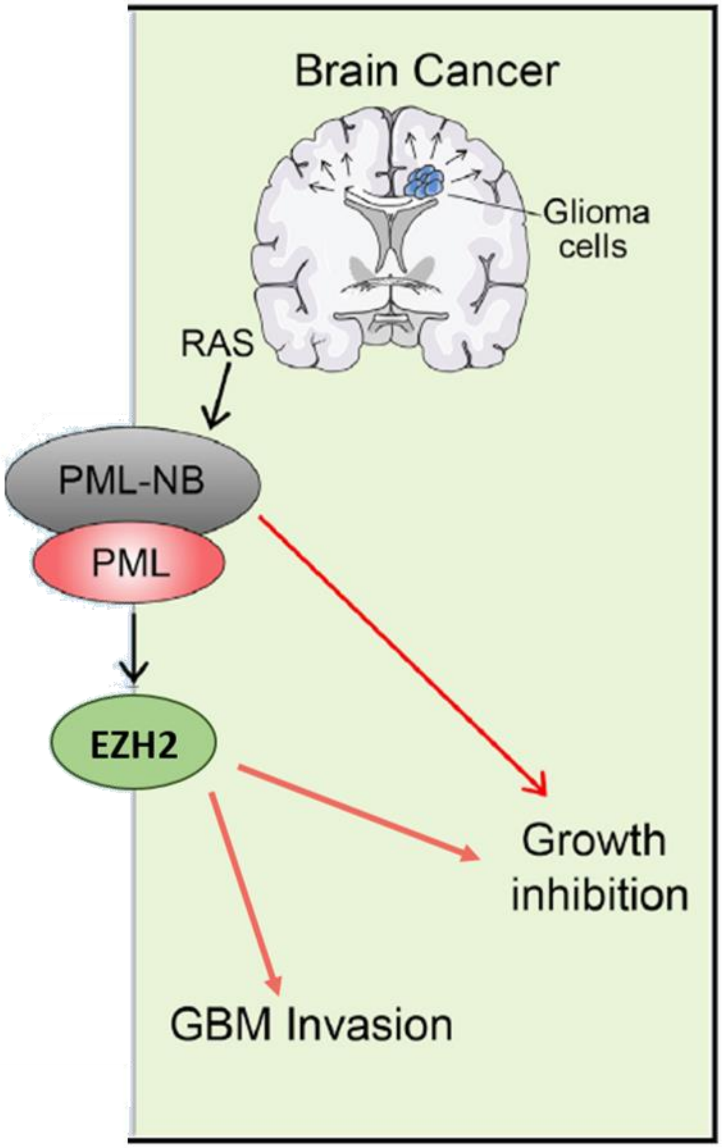

Figure 30. PML hypothesized physiological role.

The model suggests a migratory mechanism under PML overexpression. In line with the biological findings, the *in silico* simulations described PML-OE cells that have similar diffusive capability with the U87MG-PML cells, even though the growth is inhibited. In order to further explore the migratory mechanisms describing PML-invasion, we assumed that each initial tumor spheroid is composed of cells with different phenotypic traits with respect to the adhesion property (Motile:Adhesive) and we simulated the effects of the DZNeP presence. Even though the initial invasive parameters were the same for both the U87MG-PML and U87MG-PML OE cells, the Motile:Adhesive ratio phenotypes had to be further reduced in the PML-OE cells under DZNeP presence. Thus, under DZNeP presence the invading cells are inhibited. This indicates that the PML-EZH2 pathway regulates the capability of the cell to migrate in terms of making the cells more invasive and less proliferative.

5. CONCLUSIONS AND FUTURE PERSPECTIVES

Even though the invasive properties of GB have been thoroughly studied as a potential target in GB treatment, there is limited knowledge regarding the actual *in vivo* phenomenon. Many *In vitro* biological 3D experimental models try to describe the early phases of tumor progression by utilizing a variety of artificial substrates to mimic the natural microenvironment of the tumor and study the tumor-substrate interactions (Xiao et al., 2017). These approaches recapitulate morphologically and biochemically the 3D structure of the tumor extracellular matrix (ECM) embedding but they are limited in developing structural and cellular properties, such as the cellular microenvironment that is heterogeneously organized and constantly interacts with the tumor cells (Eisemann et al., 2018).

Adult murine brain slices have been proposed to retain their cytoarchitecture and authentic ECM when cultured *ex vivo* (Eisemann et al., 2018), mimicking most structural and biochemical features of the natural tumoral microenvironment (Meijer et al., 2017). Therefore, GB migration and infiltration have been previously studied *ex vivo*, by the transplantation of GB cells into rodent brain slices (Matsumura et al., 2000; Fayzullin et al., 2016; Eisemann et al., 2018). However, most *ex vivo* studies of tumor cell invasion mainly focus on the 2D distribution of the invasive cells, taking into account the spatial expansion of the invasive rim and the gradual change in the tumor core size (Matsumura et al., 2000; Fayzullin et al., 2016; Eisemann et al., 2018). Therefore, the phenomenon has been mostly described macroscopically; little evidence has been shown regarding the morphology of the invasive rim infiltration within the adjacent tissue and the anatomical structure of the infiltrated brain slice has not yet been visualized (Matsumura et al., 2000; Fayzullin et al., 2016; Eisemann et al., 2018). Moreover, while there are descriptive studies regarding the invasive behavior of established GB cell lines *in vitro*, less is known regarding the morphology of the primary GB cells distribution *in vitro* or *ex vivo.*

In order to monitor the progression of the tumor in conditions that better mimic the natural microenvironment of GB, we plan to extent these studies using an *ex vivo* experimental set up. This approach utilizes TYR-expressing 3D spheroids implanted within a live mouse brain slice. Due to the melanin production from the tumor cells and the brain tissue auto-fluorescence, the tumor expansion can be monitored using a hybrid custom made fluorescence-PA microscope. Preliminary results show the mouse brain slice auto-fluorescence detected with this technique (Figure 31). In addition to our *in vitro* results regarding the physiology and molecular mechanisms underlying GB progression, with this approach we can also gain anatomical information regarding the GB expansion within the natural tissue of GB origin.

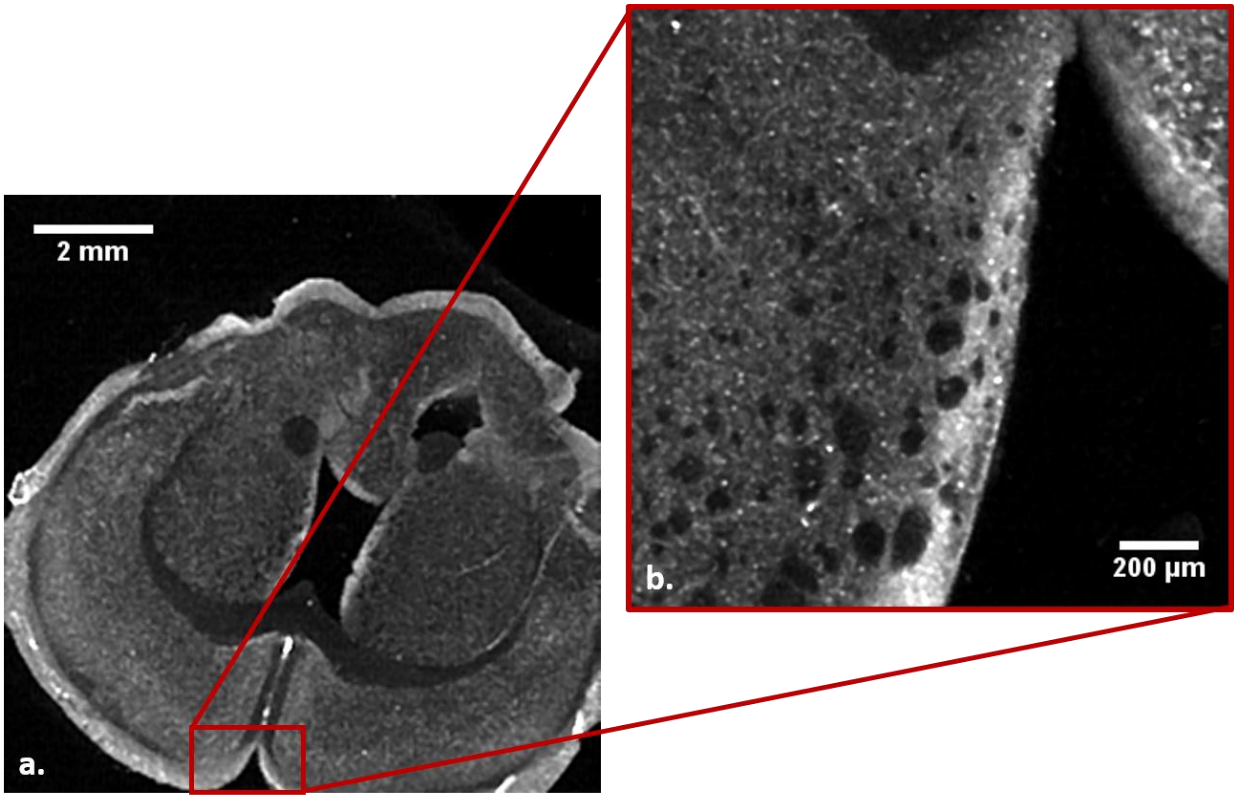

Figure 31. (a) **Mouse brain slice imaged with the hybrid custom made fluorescence-PA microscope.** (b) **Magnification at the level of the middle line. Scalebar represents 2mm and 2um respectively.**

6. THESIS LIST OF PUBLICATIONS

PUBLICATIONS

- Oraiopoulou M.E., **Tampakaki M.**, Tzamali E., Tamiolakis T., Makatounakis V., Vakis F. A., Zacharakis G., Sakkalis V., Papamatheakis J., ***"A 3D tumor spheroid model for the T98G Glioblastoma cell line phenotypic characterization"***, Tissue and Cell, Elsevier, 2019

PUBLIC ANNOUNCEMENTS

Oral Presentations

- **Tampakaki M.**, Oraiopoulou M.E., Psycharakis S., Tzamali E., Zacharakis G., Sakkalis V., Vakis A., Papamatheakis J., **(2019), "*The Physiological Effects of the Promyelocytic Leukemia Protein on the U87MG Glioblastoma Cell Line*"**, 33rd Annual Congress Hellenic Neurosurgical Society & 4th Congress SeENS Southeast Europe Neurosurgical Society, Thessaloniki, Greece

Posters

- **Tampakaki M.,** Oraiopoulou M.E., Tzamali E., Zacharakis G., Sakkalis V., Papamatheakis J., **(2019), "*The effect of pathological developmental pathways in human brain cancer physiology*"**, 28th meeting of the Hellenic Society for Neuroscience", Heraklion, Greece
- **Tampakaki M.,** Oraiopoulou M.E., Psycharakis S., Tzamali E., Sakkalis V., Zacharakis G., Papamatheakis J., **(2019)**, **"*The Role of PML in Glioblastoma Physiology*"**, 4th ESMI Imaging Summer Conference TOPIM-TECH, Chania, Greece
- **Tampakaki M.**, Oraiopoulou M.E., Psycharakis S., Tzamali E., Sakkalis V., Zacharakis G., Papamatheakis J., **(2019)**, **"*Light Sheet Fluorescence Microscopy Imaging of promyelocytic leukemia protein physiologic effects on the U87MG Glioblastoma cell line*"**, 14th European Molecular Imaging Meeting (EMIM), Glasgow, Scotland, UK

7. ACKNOWLEDGEMENTS

Καταρχάς, θα ήθελα να ευχαριστήσω τον επιβλέποντά μου Ερευνητή Δρ. κ. **Βαγγέλη Σακκαλή** για την εμπιστοσύνη που μου έδειξε, για τη συνεχή προσφορά και καθοδήγησή του από την πρώτη στιγμή που εντάχθηκα στην ομάδα, καθώς και για τις πολύτιμες συμβουλές που μου έδωσε καθ'όλη τη διάρκεια αυτής της εργασίας. Θα ήθελα, ακόμη, να ευχαριστήσω τον Καθηγητή κ. **Σήφη Παπαματθαιάκη** για τις σημαντικές συμβουλές του, ο οποίος αποτέλεσε εμπνευστή της ιδέας και συνεχίζει να αποτελεί πηγή γνώσεων και δημιουργικότητας για εμένα και την ομάδα. Ευχαριστώ, επίσης, τον Δρ. κ. **Γιάννη Ζαχαράκη**, για όλες τις ευκαιρίες που μου έδωσε να διευρύνω τους ορίζοντές μου και να με παρακινεί να βγάζω πάντα τον καλύτερό μου εαυτό. Δεν θα μπορούσα να μην ευχαριστήσω, ακόμη, τον Καθηγητή και διευθυντή της Νευροχειρουργική κλινικής του ΠΑΓΝΗ κ. **Αντώνη Βάκη**, για το συμβουλευτικό του ρόλο και τις ευκαιρίες που μου έδωσε να μάθω και να μυηθώ σε τόσα πολλά πράγματα γύρω από τη γενικότερη φύση του αντικειμένου που με ενδιαφέρει και μελετάω.

Θα ήθελα, ακόμη, να εκφράσω ένα πολύ μεγάλο ευχαριστώ στη φίλη και συντονίστρια αυτής της δουλειάς Δρ. **Μαριλένα Ωραιοπούλου**, η οποία με καθοδήγησε σε κάθε στάδιο και ήταν δίπλα μου να με στηρίζει και να με εμπνέει και της οποίας η βοήθεια ήταν καίρια για την εκπαίδευση και την εξέλιξή μου. Ακόμη, ένα μεγάλο ευχαριστώ στην Δρ. **Ελευθερία Τζαμαλή**, η οποία με συμβούλευε και με βοήθησε σε όλα τα στάδια αυτής της δουλειάς. Θα ήθελα ακόμη να ευχαριστήσω τον **Γιώργο Τζεδάκη** και **Στέλιο Ψυχαράκη**, των οποίων η συμβολή ήταν καταλυτική για την διεκπεραίωση της εργασίας. Δεν θα μπορούσα να παραλείψω να ευχαριστήσω, ακόμη, τον κ. **Τάκη Μακατουνάκη** και την κ. **Αγγέλα Πασπαράκη** για την σημαντική τους βοήθεια σε κομβικά σημεία αυτής της δουλειάς.

Θα ήθελα ακόμη να ευχαριστήσω την Επίκουρη Καθηγήτρια και μέλος της εξεταστικής επιτροπής μου Δρ. κα **Κυριακή Σιδηροπούλου** για τα εποικοδομητικά της σχόλια σε αυτήν την εργασία, καθώς και για τον καθοδηγητικό της ρόλο από τα πρώτα μου ερευνητικά βήματα. Ακόμη, οφείλω να ευχαριστήσω τον Αναπληρωτή Καθηγητή, επίσης μέλος της εξεταστικής επιτροπής μου, κ. **Θωμά Μαρή** για όλα τα εποικοδομητικά σχόλια.

Θα ήθελα τέλος να ευχαριστήσω τη μητέρα μου, τον αφανή ήρωα, για όλη της τη στήριξη και τον πατέρα μου, ο οποίος δεν είναι πια κοντά μας και μοναδική του επιθυμία ήταν να με δει να προοδεύω και έκανε τα αδύνατα δυνατά για αυτό το σκοπό. Θα ήθελα να ευχαριστήσω, ακόμη, όλη μου την οικογένεια και τους φίλους μου, που με στηρίζουν ανιδιοτελώς σε κάθε βήμα μου τόσα χρόνια.

8. REFERENCES

Aaberg-Jessen C, Norregaard A, Christensen KG, Jensen SS, Andersen C, Kristensen BW (2011) Abstract 4305: Invasion of primary glioma- and cell line-derived spheroids implanted into corticostriatal slice cultures. 6:4305–4305.

Adamski V, Schmitt AD, Flüh C, Synowitz M, Hattermann K, Held-Feindt J (2017) Isolation and characterization of fast-migrating human glioma cells in the progression of malignant gliomas. Oncol Res 25:341–353.

Akagi J, Kordon M, Zhao H, Matuszek A, Dobrucki J, Errington R, Smith PJ, Takeda K, Darzynkiewicz Z, Wlodkowic D (2013) Real-time cell viability assays using a new anthracycline derivative DRAQ7®. Cytom Part A 83 A:227–234.

Alexeyev MF, Fayzulin R, Shokolenko IN, Pastukh V (2010) A retro-lentiviral system for doxycycline-inducible gene expression and gene knockdown in cells with limited proliferative capacity. Mol Biol Rep 37:1987–1991 Available at: https://www.ncbi.nlm.nih.gov/pubmed/19655272.

Alfonso JCL, Talkenberger K, Seifert M, Klink B, Hawkins-Daarud A, Swanson KR, Hatzikirou H, Deutsch A (2017) The biology and mathematical modelling of glioma invasion: A review. J R Soc Interface 14.

Allen M, Bjerke M, Edlund H, Nelander S, Westermark B (2016) Origin of the U87MG glioma cell line: Good news and bad news. Sci Transl Med 8.

Amodeo V et al. (2017) A PML/Slit Axis Controls Physiological Cell Migration and Cancer Invasion in the CNS. Cell Rep 20:411–426 Available at: http://dx.doi.org/10.1016/j.celrep.2017.06.047.

Anderson ARA (2005) A hybrid mathematical model of solid tumour invasion: the importance of cell adhesion. Math Med Biol A J IMA 22:163–186 Available at: https://doi.org/10.1093/imammb/dqi005.

Anderson ARA, Rejniak KA, Gerlee P, Quaranta V (2007) Modelling of cancer growth, evolution and invasion: Bridging scales and models. Math Model Nat Phenom 2:1–29.

Anderson ARA, Weaver AM, Cummings PT, Quaranta V (2006) Tumor Morphology and Phenotypic Evolution Driven by Selective Pressure from the Microenvironment. Cell 127:905–915.

Aum DJ, Kim DH, Beaumont TL, Leuth EC, Dunn GP, Kim AH (2015) Molecular and cellular heterogeneity: the hallmark of glioblastoma. Therm Phys 37:559–564.

Ballesta A, Zhou Q, Zhang X, Lv H, Gallo JM (2014) Multiscale Design of Cell-Type–Specific Pharmacokinetic/Pharmacodynamic Models for Personalized Medicine: Application to Temozolomide in Brain Tumors. CPT Pharmacometrics Syst Pharmacol 3:e112 Available at: http://doi.wiley.com/10.1038/psp.2014.9.

Bernardi R, Pandolfi PP (2007) Structure, dynamics and functions of promyelocytic leukaemia nuclear bodies. Nat Rev Mol Cell Biol 8:1006–1016.

Bernas T, Zarębski M, Cook RR, Dobrucki JW (2004) Minimizing photobleaching during confocal microscopy of fluorescent probes bound to chromatin: Role of anoxia and photon flux. J Microsc 215:281–296.

Blockus H, Chédotal A (2014) The multifaceted roles of Slits and Robos in cortical circuits: From proliferation to axon guidance and neurological diseases. Curr Opin Neurobiol.

Bogdańska MU, Bodnar M, Belmonte-Beitia J, Murek M, Schucht P, Beck J, Pérez-García VM (2017) A mathematical model of low grade gliomas treated with temozolomide and its therapeutical implications. Math Biosci 288:1–13.

Bonavia R, Inda MDM, Cavenee WK, Furnari FB (2011) Heterogeneity maintenance in glioblastoma: A social network. Cancer Res 71:4055–4060.

Claes A, Idema AJ, Wesseling P (2007) Diffuse glioma growth: A guerilla war. Acta Neuropathol 114:443–458.

Clendenon SG, Young PA, Ferkowicz M, Phillips C, Dunn KW (2011) Deep tissue fluorescent imaging in scattering specimens using confocal microscopy. Microsc Microanal 17:614–617.

Crowley LC, Marfell BJ, Christensen ME, Waterhouse NJ (2016) Measuring cell death by trypan blue uptake and light microscopy. Cold Spring Harb Protoc 2016:643–646.

Cuddapah VA, Robel S, Watkins S, Sontheimer H (2014) A neurocentric perspective on glioma invasion. Nat Rev Neurosci 15:455–465 Available at: http://dx.doi.org/10.1038/nrn3765.

Dixit R, Cyr R (2003) Cell damage and reactive oxygen species production induced by fluorescence microscopy: Effect on mitosis and guidelines for non-invasive fluorescence microscopy. Plant J 36:280–290.

Eisemann T, Costa B, Strelau J, Mittelbronn M, Angel P, Peterziel H (2018) An advanced glioma cell invasion assay based on organotypic brain slice cultures. BMC Cancer 18:1–10.

Faiz M, Sachewsky N, Gascón S, Bang KWA, Morshead CM, Nagy A (2015) Adult Neural Stem Cells from the Subventricular Zone Give Rise to Reactive Astrocytes in the Cortex after Stroke. Cell Stem Cell 17:624–634.

Fayzullin A, Tuvnes FA, Skjellegrind HK, Behnan J, Mughal AA, Langmoen IA, Vik-Mo EO (2016) Time-lapse phenotyping of invasive glioma cells ex vivo reveals subtype-specific movement patterns guided by tumor core signaling. Exp Cell Res 349:199–213 Available at: http://dx.doi.org/10.1016/j.yexcr.2016.08.001.

Foty R (2011) A Simple Hanging Drop Cell Culture Protocol for Generation of 3D Spheroids. J Vis Exp 20:4–7.

Girard N, Bazille C, Lhuissier E, Benateau H, Llombart-Bosch A, Boumediene K, Bauge C (2014) 3-Deazaneplanocin A (DZNep), an inhibitor of the histone methyltransferase EZH2, induces apoptosis and reduces cell migration in chondrosarcoma cells. PLoS One 9:3–10.

Greger K, Swoger J, Stelzer EHK (2007) Basic building units and properties of a fluorescence single plane illumination microscope. Rev Sci Instrum 78.

Grotzer MA, Neve A, Baumgartner M (2016) Dissecting brain tumor growth and metastasis in vitro and ex vivo. J Cancer Metastasis Treat 2:149 Available at: http://jcmtjournal.com/article/view/1488.

Guan D, Kao HY (2015) The function, regulation and therapeutic implications of the tumor suppressor protein, PML. Cell Biosci 5.

Gurrieri C, Capodieci P, Bernardi R, Scaglioni PP, Nafa K, Rush LJ, Verbel DA, Cordon-Cardo C, Pandolfi PP (2004) Loss of the tumor suppressor PML in human cancers of multiple histologic origins. J Natl Cancer Inst 96:269–279.

Hambsch P, Istomin YP, Tzerkovsky DA, Patties I, Neuhaus J, Kortmann R-D, Schastak S, Glasow A (2017) Efficient cell death induction in human glioblastoma cells by photodynamic treatment with Tetrahydroporphyrin-Tetratosylat (THPTS) and ionizing irradiation. Oncotarget 8:72411–72423.

Hanif F, Muzaffar K, Perveen K, Malhi SM, Simjee SU (2017) Glioblastoma Multiforme: A Review of its Epidemiology and Pathogenesis through Clinical Presentation and Treatment. Asian Pac J Cancer Prev 18:3–9 Available at: http://www.ncbi.nlm.nih.gov/pubmed/28239999%0Ahttp://www.pubmedcentral.nih.gov/articlerender.fcgi?artid=PMC5563115%0Ahttp://www.ncbi.nlm.nih.gov/pubmed/28239999%0Ahttp://www.pubmedcentral.nih.gov/articlerender.fcgi?artid=PMC5563115%0Ahttp://www.ncbi.nlm.n.

Holland EC (2000) Glioblastoma multiforme: The terminator. Proc Natl Acad Sci 97:6242–6244 Available at: http://www.pnas.org/cgi/doi/10.1073/pnas.97.12.6242.

Hou LC, Veeravagu A, Hsu AR, Tse VCK (2006) Recurrent glioblastoma multiforme: a review of natural history and management options. Neurosurg Focus FOC 20:E3 Available at: https://thejns.org/focus/view/journals/neurosurg-focus/20/4/foc.2006.20.4.2.xml.

Hsu KS, Kao HY (2018) PML: Regulation and multifaceted function beyond tumor suppression. Cell Biosci 8:1–21 Available at: https://doi.org/10.1186/s13578-018-0204-8.

Imani-Saber Z, Ghafouri-Fard S (2014) Promyelocytic leukemia gene functions and roles in tumorigenesis. Asian Pacific J Cancer Prev 15:8021–8028.

Iwanami A, Gini B, Zanca C, Matsutani T, Assuncao A, Nael A, Dang J, Yang H, Zhu S, Kohyama J, Kitabayashi I, Cavenee WK, Cloughesy TF, Furnari FB, Nakamura M, Toyama Y, Okano H, Mischel PS (2013) PML mediates glioblastoma resistance to mammalian target of rapamycin (mTOR)-targeted therapies. Proc Natl Acad Sci 110:4339–4344 Available at: http://www.pnas.org/lookup/doi/10.1073/pnas.1217602110.

Jensen K, Shiels C, Freemont PS (2001) PML protein isoforms and the RBCC / TRIM motif.

Kalinski P (2017) Tumor immune microenvironment in cancer progression and cancer therapy.

Kam Y, Rejniak KA, Anderson ARA (2012) Cellular modeling of cancer invasion: integration of in silico and in vitro approaches. J Cell Physiol 227:431–438 Available at: https://www.ncbi.nlm.nih.gov/pubmed/21465465.

Kaneko N, Marín O, Koike M, Hirota Y, Uchiyama Y, Wu JY, Lu Q, Tessier-Lavigne M, Alvarez-Buylla A, Okano H, Rubenstein JLR, Sawamoto K (2010) New neurons clear the path of astrocytic processes for their rapid migration in the adult brain. Neuron.

Karlas A, Fasoula N-A, Paul-Yuan K, Reber J, Kallmayer M, Bozhko D, Seeger M, Eckstein H-H, Wildgruber M, Ntziachristos V (2019) Cardiovascular optoacoustics: From mice to men – A review. Photoacoustics 14:19–30 Available at: http://www.sciencedirect.com/science/article/pii/S2213597919300230.

Kiseleva LN, Kartashev A V., Vartanyan NL, Pinevich AA, Filatov M V., Samoilovich MP (2018) Characterization of New Human Glioblastoma Cell Lines. Cell tissue biol 12.

Klinghammer K, Walther W, Hoffmann J (2017) Choosing wisely – Preclinical test models in the era of precision medicine. Cancer Treat Rev 55:36–45 Available at: http://dx.doi.org/10.1016/j.ctrv.2017.02.009.

Koh I, Cha J, Park J, Choi J, Kang SG, Kim P (2018) The mode and dynamics of glioblastoma cell invasion into a decellularized tissue-derived extracellular matrix-based three-dimensional tumor model. Sci Rep 8:1–12 Available at: http://dx.doi.org/10.1038/s41598-018-22681-3.

Lallemand-Breitenbach V, De The H (2010) PML Nuclear Bodies. :1–17.

Larjavaara S, Mantyla R, Salminen T, Haapasalo H, Raitanen J, Jaaskelainen J, Auvinen A (2007) Incidence of gliomas by anatomic location. Neuro Oncol 9:319–325 Available at: https://academic.oup.com/neuro-oncology/article-lookup/doi/10.1215/15228517-2007-016.

Larson B (2015) BioTek White Paper - 3D Cell Culture: A Review of Current Techniques. WwwBiotekCom 6:1–10.

Lee HE, Jee C Do, Kim MA, Lee HS, Lee YM, Lee BL, Kim WH (2007) Loss of promyelocytic leukemia protein in human gastric cancers. Cancer Lett 247:103–109.

Leung BM, Lesher-Perez SC, Matsuoka T, Moraes C, Takayama S (2015) Media additives to promote spheroid circularity and compactness in hanging drop platform. Biomater Sci 3:336–344.

Lorenzo C, Frongia C, Jorand R, Fehrenbach J, Weiss P, Maandhui A, Gay G, Ducommun B, Lobjois V (2011) Live cell division dynamics monitoring in 3D large spheroid tumor models using light sheet microscopy. Cell Div 6:22.

Louis DN, Perry A, Reifenberger G, von Deimling A, Figarella-Branger D, Cavenee WK, Ohgaki H, Wiestler OD, Kleihues P, Ellison DW (2016) The 2016 World Health Organization Classification of Tumors of the Central Nervous System: a summary. Acta Neuropathol 131:803–820.

Magidson V, Khodjakov A (2013) Circumventing photodamage in live-cell microscopy. Methods Cell Biol 114:545–560.

Mallawaaratchy DM, Buckland ME, McDonald KL, Li CCY, Ly L, Sykes EK, Christopherson RI, Kaufman KL (2015) Membrane Proteome Analysis of Glioblastoma Cell Invasion. J Neuropathol Exp Neurol 74:425–441.

Margueron R, Reinberg D (2011) The Polycomb complex PRC2 and its mark in life. Nature 469:343 Available at: https://doi.org/10.1038/nature09784.

Martín-Martín N et al. (2016) Stratification and therapeutic potential of PML in metastatic breast cancer. Nat Commun 7.

Matsumura H, Ohnishi T, Kanemura Y, Maruno M, Yoshimine T (2000) Quantitative analysis of glioma cell invasion by confocal laser scanning microscopy in a novel brain slice model. Biochem Biophys Res Commun 269:513–520.

Mazza M, Pelicci PG (2013) Is PML a Tumor Suppressor? Front Oncol 3:1–9.

McKenna MT, Weis JA, Barnes SL, Tyson DR, Miga MI, Quaranta V, Yankeelov TE (2017) A Predictive Mathematical Modeling Approach for the Study of Doxorubicin Treatment in Triple Negative Breast Cancer. Sci Rep 7:1–14 Available at: http://dx.doi.org/10.1038/s41598-017-05902-z.

Mehrmohammadi M, Yoon SJ, Yeager D, Emelianov SY (2013) Photoacoustic Imaging for Cancer Detection and Staging. Curr Mol Imaging 2:89–105.

Meijer TG, Naipal KA, Jager A, van Gent DC (2017) Ex vivo tumor culture systems for functional drug testing and therapy response prediction. Futur Sci OA 3:FSO190 Available at: http://www.ncbi.nlm.nih.gov/pubmed/28670477%0Ahttp://www.pubmedcentral.nih.gov/articlerender.fcgi?artid=PMC5481868.

Montana V (2016) Glioma: the Mechanisms of Infiltrative Growth. Opera Medica Physiol 2:69–76 Available at: http://www.operamedphys.org/OMP_2016_01_0025.

Mullins CS, Schneider B, Stockhammer F, Krohn M, Classen CF, Linnebacher M (2013) Establishment and Characterization of Primary Glioblastoma Cell Lines from Fresh and Frozen Material: A Detailed Comparison. PLoS One 8.

Nisole S, Maroui MA, Mascle XH, Aubry M, Chelbi-Alix MK (2013) Differential Roles of PML Isoforms. Front Oncol 3:1–17.

Nørøxe DS, Poulsen HS, Lassen U (2016) Hallmarks of glioblastoma: A systematic review. ESMO Open 1:1–9.

Ntziachristos V (2010) Going deeper than microscopy: the optical imaging frontier in biology. Nat Methods 7:603 Available at: https://doi.org/10.1038/nmeth.1483.

Ohgaki H, Kleihues P (2013) The definition of primary and secondary glioblastoma. Clin Cancer Res 19:764–772.

Oraiopoulou M-E, Tzamali E, Tzedakis G, Liapis E, Zacharakis G, Vakis A, Papamatheakis J, Sakkalis V (2018) Integrating in vitro experiments with in silico approaches for Glioblastoma invasion: the role of cell-to-cell adhesion heterogeneity. Sci Rep 8:16200 Available at: https://doi.org/10.1038/s41598-018-34521-5.

Oraiopoulou ME, Tzamali E, Tzedakis G, Vakis A, Papamatheakis J, Sakkalis V (2017) In Vitro/In silico study on the role of doubling time heterogeneity among primary glioblastoma cell lines. Biomed Res Int 2017.

Ovsepian S V., Olefir I, Westmeyer G, Razansky D, Ntziachristos V (2017) Pushing the Boundaries of Neuroimaging with Optoacoustics. Neuron 96:966–988 Available at: https://doi.org/10.1016/j.neuron.2017.10.022.

Previati M, Missiroli S, Perrone M, Caroccia N, Paliotto F, Milani D, Giorgi C (2018) Functions and dys-functions of promyelocytic leukemia protein PML. Rend Lincei 29:411–420 Available at: https://doi.org/10.1007/s12210-018-0714-7.

Psycharakis SE, Liapis E, Zacharopoulos A, Oraiopoulou ME, Papamatheakis J, Sakkalis V, Zacharakis G (2018) High resolution volumetric imaging of primary and secondary tumor spheroids using multi-angle Light Sheet Fluorescence Microscopy (LSFM). Proc Annu Int Conf IEEE Eng Med Biol Soc EMBS 2018-July:866–869.

Ramão A, Gimenez M, Laure HJ, Izumi C, Vida RCDS, Oba-Shinjo S, Marie SKN, Rosa JC (2012) Changes in the expression of proteins associated with aerobic glycolysis and cell migration are involved in tumorigenic ability of two glioma cell lines. Proteome Sci 10:1–12.

Regad T, Bellodi C, Nicotera P, Salomoni P (2009) The tumor suppressor Pml regulates cell fate in the developing neocortex. Nat Neurosci 12:132–140.

Rieger AM, Nelson KL, Konowalchuk JD, Barreda DR (2011) Modified Annexin V / Propidium Iodide Apoptosis Assay For Accurate Assessment of Cell Death. :3–6.

Rosa J De, Iraburu M, Gallo-oller G, Shahi MH, Meléndez B, Rey JA, Idoate MA, Castresana JS (2016) EZH2 as a Therapeutic Target in Glioblastoma : A Cellular and Molecular Study Carcinogenesis Car cinogenesis & Mutagenesis. 7:6–13.

Sachini N, Arampatzi P, Klonizakis A, Nikolaou C, Makatounakis T, Lam EWF, Kretsovali A, Papamatheakis J (2019) Promyelocytic leukemia protein (PML) controls breast cancer cell proliferation by modulating Forkhead transcription factors. Mol Oncol 13:1369–1387.

Santi PA (2011) Light sheet fluorescence microscopy: A review. J Histochem Cytochem 59:129–138.

Smits M, Mir SE, Nilsson RJA, Stoop PM Van Der, Niers JM, Marquez VE, Cloos J, Breakefield XO, Krichevsky AM, Noske DP (2011) Down-Regulation of miR-101 in Endothelial Cells Promotes Blood Vessel Formation through Reduced Repression of EZH2. 6.

Stein GH (1979) T98G: An anchorage-independent human tumor cell line that exhibits stationary phase G1 arrest in vitro. J Cell Physiol 99:43–54 Available at: https://doi.org/10.1002/jcp.1040990107.

Sun XX, Yu Q (2015) Intra-tumor heterogeneity of cancer cells and its implications for cancer treatment. Acta Pharmacol Sin 36:1219–1227 Available at: http://dx.doi.org/10.1038/aps.2015.92.

Swanson KR, Rockne RC, Claridge J, Chaplain MA, Alvord EC, Anderson ARA (2011) Quantifying the Role of Angiogenesis in Malignant Progression of Gliomas: In Silico Modeling Integrates Imaging and Histology. Cancer Res 71:7366 LP – 7375 Available at: http://cancerres.aacrjournals.org/content/71/24/7366.abstract.

Taruttis A, Van Dam GM, Ntziachristos V (2015) Mesoscopic and macroscopic optoacoustic imaging of cancer. Cancer Res 75:1548–1559.

Tserevelakis GJ, Avtzi S, Tsilimbaris MK, Zacharakis G (2017) Delineating the anatomy of the ciliary body using hybrid optical and photoacoustic imaging. J Biomed Opt 22:060501.

Tserevelakis GJ, Tsagkaraki M, Zacharakis G (2016) Hybrid photoacoustic and optical imaging of pigments in vegetative tissues. J Microsc 263:300–306.

van Meerloo J, Kaspers GJL, Cloos J (2011) Cell Sensitivity Assays: The MTT Assay. In: Cancer Cell Culture: Methods and Protocols (Cree IA, ed), pp 237–245. Totowa, NJ: Humana Press. Available at: https://doi.org/10.1007/978-1-61779-080-5_20.

Verveer PJ, Swoger J, Pampaloni F, Greger K, Marcello M, Stelzer EHK (2007) High-resolution three-dimensional imaging of large specimens with light sheet–based microscopy. Nat Methods 4:311–313 Available at: https://doi.org/10.1038/nmeth1017.

Wu D, Yotnda P (2011) Production and detection of reactive oxygen species (ROS) in cancers. J Vis Exp:3357 Available at: https://www.ncbi.nlm.nih.gov/pubmed/22127014.

Xiao W, Sohrabi A, Seidlits SK (2017) Integrating the glioblastoma microenvironment into engineered experimental models. Futur Sci OA 3:FSO189 Available at: http://www.ncbi.nlm.nih.gov/pubmed/28883992%0Ahttp://www.pubmedcentral.nih.gov/articlerender.fcgi?artid=PMC5583655.

Zada G, Bond AE, Wang YP, Giannotta SL, Deapen D (2012) Incidence trends in the anatomic location of primary malignant brain tumors in the United States: 1992-2006. World Neurosurg 77:518–524 Available at: http://dx.doi.org/10.1016/j.wneu.2011.05.051.

Zong H, Parada LF, Baker SJ (2015) Cell of origin for malignant gliomas and its implication in therapeutic development. Cold Spring Harb Perspect Biol 7:a020610 Available at: https://www.ncbi.nlm.nih.gov/pubmed/25635044.

Zou C, Wu B, Dong Y, Song Z, Zhao Y, Ni X, Yang Y, Liu Z (2017) Biomedical photoacoustics: Fundamentals, instrumentation and perspectives on nanomedicine. Int J Nanomedicine 12:179–195.